Development of Superconducting Single-Photon and Photon-Number Resolving Detectors for Quantum Applications

Adriana E. Lita, Dileep V. Reddy, *Member, IEEE*, Varun B. Verma, Richard P. Mirin, *Fellow, IEEE*, and Sae Woo Nam, *Fellow, IEEE*

(Integrated Photonics 2022)

***Abstract*—Single-photon detectors based on superconducting thin films have become a viable class of technologies for widespread usage in quantum optics. In this tutorial paper we introduce the key performance metrics required of them for quantum information processing and related fields. We review the latest records achieved by such devices, study technical details regarding recent improvements in superconducting nanowire detectors and transition-edge sensors, and present representative applications in cutting-edge research areas that benefit from these advances.**

***Index Terms*—Nanophotonics, quantum optics, superconducting devices, superconducting photodetectors, superconducting wires.**

I. Introduction to Superconducting Single-Photon Detectors

ONE of the enabling technologies for all photonic quantum applications is single-photon detection. Superconductivity-based approaches of single-photon detectors require operation at significantly below room temperature which, although an engineering challenge, has built-in strong suppression of many of the noise processes (false counts) that can interfere with efficient detection of single photons. In recent years, significant advances in cryogenic systems have yielded turn-key systems for operating at down to hundreds of mK temperatures [1], making it more common for an optics lab to routinely operate superconducting detectors.

A superconducting radiation sensor's operating principle is based on exploiting the transition between the superconducting state and the normal state that occurs in superconducting materials [2]. The superconducting state is a distinct thermodynamic phase that exists only when temperature, external magnetic field and the current density carried by the material are below critical values denoted as T_c, the critical temperature of the material, H_c, the critical magnetic field, and J_c, the critical value of the current density.

The superconducting transition is associated with the presence of an energy gap between the ground state and electronic excited states. In the superconducting ground state, the electrons are paired up into superconducting charge carriers, called Cooper pairs [3], with binding energy of 2Δ, due to weak attractive interaction caused by phonon emission/absorption. When energy is absorbed by the superconductor (for example from a sufficiently energetic photon), the Cooper pairs dissociate into electrons excited out of the ground state, known as "quasiparticles". Typically, the superconducting energy gap Δ for quasiparticle excitation is orders of magnitude smaller than the energy of an optical photon (meV versus eV). So a single photon in the visible or near-infrared can create hundreds or thousands of quasiparticle excitations. Counting the number of quasiparticle excitations following a single-photon absorption event proved to be a successful detection method used in Superconducting Tunnel Junction (STJ) and Kinetic Inductance Detectors (KIDs). An alternative to counting quasiparticle excitations is a microcalorimeter based energy-resolving detector, such as the Transition-Edge Sensor (TES), that can measure the temperature change that follows the absorption of a single photon with an exquisitely sensitive thermometer [4]. And finally, the characteristic switching of a superconducting material at a fixed temperature when the current density exceeds the "critical" value of the current density, J_c, has been exploited to implement the Superconducting Nanowire Single-Photon Detector (SNSPD) or Superconducting Nanostrip Photon Detector [5].

Following the first demonstration of single optical photon detection [6] with a superconducting device, namely STJ, there has been a lot of research focused on developing superconducting single-photon detectors with increased performance over conventional semiconductor-based detectors and photomultiplier tubes. Superconducting detectors can outperform conventional photon-counting technologies in a variety of performance metrics such as detection efficiency, dark count rate, timing jitter, recovery time, and energy resolution. The most successful technologies have been: TESs, SNSPDs, KIDs and STJs,

Manuscript received 13 June 2022; revised 25 July 2022; accepted 26 July 2022. Date of publication 29 July 2022; date of current version 16 December 2022. This work was supported by NIST, an agency of the U.S. Government. *(Corresponding author: Adriana E. Lita.)*

Adriana E. Lita, Varun B. Verma, Richard P. Mirin, and Sae Woo Nam are with the National Institute of Standards and Technology, Boulder, CO 80305 USA (e-mail: adriana.lita@nist.gov; varun.verma@nist.gov; richard.mirin@nist.gov; saewoo.nam@nist.gov).

Dileep V. Reddy is with the National Institute of Standards and Technology, Boulder, CO 80305 USA, and also with the Department of Physics, University of Colorado, Boulder, CO 80305 USA (e-mail: dileep.reddy@nist.gov).

Color versions of one or more figures in this article are available at https://doi.org/10.1109/JLT.2022.3195000.

Digital Object Identifier 10.1109/JLT.2022.3195000

TABLE I
RECORD PERFORMANCE FOR DIFFERENT SUPERCONDUCTING DETECTOR TECHNOLOGIES.

Figure of Merit	TES	SNSPD	STJ	MKID
Efficiency	95 % (1556 nm) [19], 98 % (850 nm) [31]	98 % [32], [33], 99.5 % [34]	70 % (150-600 nm), 20 % (1 μm) [8]	17 % [35]
Number resolution*	29 (1570 nm) [36], 16 (802 nm) [37]	≥ 4 [38], [39], ≥ 6 [40]	R ∼ 14 (500 nm) [8]	7 (1550 nm) [13], R ∼ 8 (400 nm [35], 808 nm [12])
Recovery time	75 ns (940 nm) [41]	80 ps† [42]	20 μs [8]	50 μs (254 nm) [35]
Timing jitter	30 ns [43], 2 ns (700 nm) [44]	2.6 ps (532 nm) [26]	1 μs [8]	1 μs (1550 nm)
Dark counts (per sec.)	0.06 [37], 0.0086 [45]	0.1‡ [46], 0.01‡ [47]	/	/
Maximum count rate	10^5 counts/s [31], [48]	1.5×10^9 counts/s [25]	10^4 counts/s [9]	2×10^3 counts/s [35]
Number of "pixels"	36 [49]	1024 [50]	120 [9]	2024 [35], 20,440 [12]

*Maximum distinguishable photon number; $R = E/\Delta E$ is the spectral resolving power.
†Among devices that are not a single straight segment of nanostrip.
‡At bias current where efficiency saturates.

which we briefly introduce in the following, along with the principle figures of merit for single-photon detectors for quantum information applications. In Section II we review present state-of-the-art advancements in performance metrics enumerated in the previous section with a focus on TESs and SNSPDs, which outperformed the other technologies. In Section III, a few quantum applications benefiting from high performance single-photon detectors are presented.

A. Superconducting Tunnel Junctions (STJ)

Superconducting tunnel junction detectors (STJs) were the pioneering devices in superconductor-based optical single-photon detection [6]. The STJs consist of two pieces of superconducting material separated by a very thin (∼nm) insulating layer. They are also known as superconductor-insulator-superconductor tunnel junctions (SIS) and represent a type of a Josephson junction [7]. Cooper pairs can tunnel across the insulating barrier, a phenomenon known as the Josephson effect. Quasiparticles can also tunnel across the barrier, although the quasiparticle current is suppressed for voltages below twice the superconducting energy gap. A photon absorbed on one side of an STJ breaks Cooper pairs and creates excess quasiparticles. In the presence of an applied voltage across the junction, the quasiparticles tunnel across the junction, and the resulting excess tunneling current is proportional to the photon energy. Hence, STJs are intrinsically energy resolving.

The energy resolution of optical and soft X-ray STJ detectors approaches the fundamental limits set by statistical fluctuations of quasiparticle generation and tunneling [8]. Hence, optical astronomy applications, particularly spectroscopy of faint optical sources, have been the main driver behind the development of STJ detectors. The European Space Agency (ESA) has operated a superconducting single-photon camera since 1999. The current S-Cam3 uses a 10×12 pixel array operating on the wavelength band of 340 nm to 740 nm, with average energy resolution of 0.17 eV at 2.4 eV (500 nm) [9]. The energy resolution is defined as the full width at half maximum (FWHM) of the statistical curve for repeated measurements at fixed photon energy, in this case 2.4 eV. Table I shows record performance for STJ devices in comparison with other detector technologies. Recently there has been renewed interest in junction-based quantum detectors. For example, near-IR single-photon detection was demonstrated with a graphene-based Josephson junction device [10].

B. Kinetic-Inductance Detector (KID)

The Kinetic Inductance Detector (KID) is based on measuring the change in kinetic inductance caused by the absorption of photons in a thin strip of superconducting material. When a photon is absorbed by a superconducting film it breaks Cooper pairs and generates quasiparticle excitations. The change in quasiparticle density changes the total surface impedance of the superconducting film. The change in inductance is typically measured as the change in the resonant frequency of a microwave resonator. In such a device a superconducting thin film is patterned in a way to form a high-Q resonator. The resonator is capacitively coupled to a feed line allowing a probe signal to be transmitted through the device: probe signals are typically a few GHz, and hence these detectors are also known as Microwave Kinetic Inductance Detectors, or MKIDs. As the quasiparticle density changes after the absorption of a photon, the corresponding change in the surface impedance alters the amplitude and the phase of the probe signal transmitted through the circuit. The MKIDs therefore, have intrinsic photon-number resolution and energy-resolving power. Their resonator-based readout is useful for developing large-format detector arrays, as each KID can be addressed by a single microwave tone and many detectors can be measured using a single broadband microwave channel, a technique known as frequency-division multiplexing.

Initially, KIDs have been developed for mm and sub-mm wavelength detection for astronomy applications, and later extended to include optical and near-infrared detection with large arrays of a few kilopixels for astronomical telescopes [11], [12]. Recently, a group at NIST [13] has shown improved single-photon counting at 1550 nm wavelength resolving up to 7 photons with energy resolution ∼0.22 eV in TiN based MKIDs. Both Hf and PtSi-based MKIDS have also shown single-photon response at optical and IR wavelengths [12], [14].

C. Transition-Edge Sensor (TES)

Superconducting transition-edge sensors (TES) are highly-sensitive microcalorimeters that have been widely used to detect radiation from sub-mm wavelengths to gamma-rays in astronomy-based applications [15], [16]. A microcalorimeter typically consists of an absorber coupled to an extremely sensitive thermometer and both are weakly linked to a heat sink kept at a constant temperature. The weak link is characterized by its thermal conductance (G), which is designed to ensure efficient excess heat removal. In general, once photons are absorbed, their energy is converted into heat, causing an increase in the absorber temperature. Subsequently the absorber temperature equilibrates to the heat sink temperature with a time constant $\tau = C/G$, where C is the TES heat capacity.

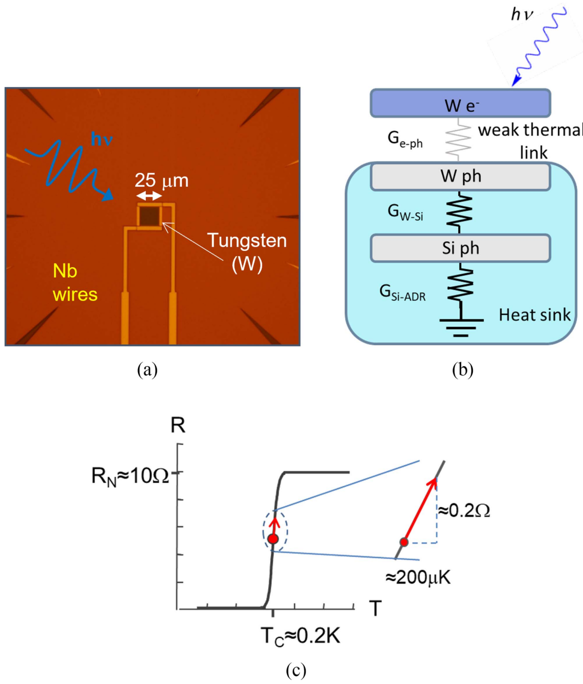

Fig. 1. (a) Optical micrograph of a typical W TES detector deposited directly on a Si wafer. (b) W TES thermal model with W electrons representing both the absorber and thermometer; the weak thermal link is modeled as a weak electron-phonon coupling in the W thin film and the heat sink is the W phonon system which is strongly coupled to the lattice of the silicon substrate and also to the cryostat cold stage onto which the detector chip is mounted. (c) Illustration of the steep transition between normal and superconducting phase of a superconductor and the measurable change in resistance at the absorption of a single optical photon.

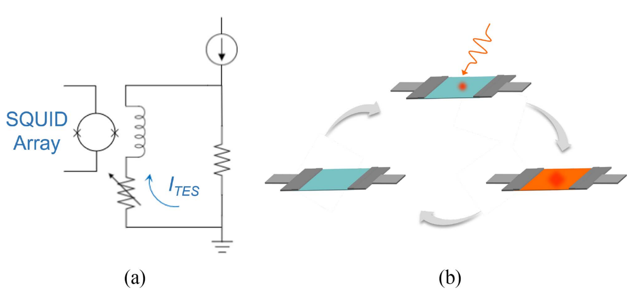

Fig. 2. Schematic of TES electrical circuit. (a) The current through the TES is measured using a SQUID array amplifier circuit while electrothermal feedback concurrently returns the device to equilibrium. (b) Representation of TES operating principle: at the absorption of a photon the TES temperature rises and is returned quickly to equilibrium by electrothermal feedback.

When a thin film of superconducting material is thermally balanced in its superconducting-to-normal transitional state, a very small change in the temperature, caused by absorption of a single optical photon, can cause a significant variation in its electrical resistivity (see Fig. 1(c)), acting as an extremely sensitive thermometer.

The optical TES developed at NIST typically consists of a tungsten (W) thin film of approximately 20 nm thickness, sputter deposited on a Si wafer (Fig. 1(a)). The electrons in tungsten are both the absorber and the thermometer and the weak thermal link is characterized by the coupling between the electron and phonon systems ($G_{\text{e-ph}}$) in the tungsten film (Fig. 1(b)).

The readout circuit of the TES is schematically depicted in Fig. 2(a). The TES is shown as a variable resistor in parallel with a shunt resistor with a value much smaller than the TES resistance when biased for photon detection. Voltage biasing of the TES ensures stable operation within the superconducting transition [15]. The sensor temperature is maintained within its superconducting-to-normal transition via Joule heating associated with the constant voltage bias (V_{bias}), a process called electrothermal feedback (ETF). The current through the TES is measured using an array of superconducting quantum interference device (SQUID) [17] amplifier circuits while electrothermal feedback concurrently returns the device to equilibrium. The SQUID input coil inductively couples the TES current (I_{TES}) via a magnetic flux to the SQUID and therefore allows direct equivalent-current readout.

When a photon is absorbed, it heats up the tungsten e^- system. This heat in excess of the Joule heating at equilibrium is removed in the form of a drop in the Joule power dissipation, such that the system restabilizes around the operating point (Fig. 2(b)). This balancing effect, known as negative ETF, significantly decreases the pulse recovery time constant [18] $\tau_{\text{etf}} = \tau/(1+\alpha/n)$, where $\alpha = (T/R)(dR/dT)$ is a dimensionless measure of the slope or steepness of the superconducting transition and n is the power-law dependence of the thermal conductance between the superconducting film and the heat sink.

The value of α depends on the nature of the weak thermal link as well as the superconducting materials used. α can be as high as 1,000 [15] and can result in a reduction of the pulse duration by two orders of magnitude compared to intrinsic film time constants, enabling pulse decay times on the order of $\sim 1\ \mu$s [19].

The optical energy deposited in the absorber (tungsten e^- system) can be calculated by multiplying the time integral of the change in current by the bias voltage. Absorption of two photons causes a temperature rise that is ideally twice that for a single photon. As a result, the TES generates an output signal that is proportional to the cumulative energy in an absorption event. This proportional pulse-height enables the determination of the energy absorbed by the TES and the direct conversion of sensor pulse-height into photon number.

TES detectors can be multiplexed in the time or frequency domain as previously shown for submillimeter astronomy applications [20], [21] reaching arrays sized of a few kilo-pixels. However, for optical and near-IR TES detectors, 36-pixel array is the largest array size to date (Table I).

D. Superconducting Nanowire Single-Photon Detector (SNSPD)

The basic operating principle of an SNSPD is shown in Fig. 3(a). The sensor element is a narrow (80–200 nm) and thin (2–5 nm) superconducting wire typically patterned on a substrate in a meandering fashion to fill the active area. Highly-disordered superconductors are typically chosen, such as NbN, WSi, or MoSi. The wire is cooled below its superconducting transition temperature and biased with a constant current. When a photon is absorbed in the material, Cooper pairs are broken, resulting in a localized normal (non-superconducting) region called a “hotspot.” This normal region then grows due to current-crowding-induced local increase in current density in excess of the critical current density of the film. Recent experiments have also shown evidence for “vortex-assisted” growth of the initial hotspot, in which tunneling of a magnetic vortex across

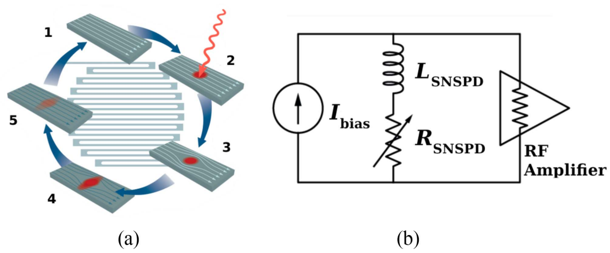

Fig. 3. (a) Conceptual representation of the operating principle of an SNSPD. The details are explained in the text. (b) Schematic of a typical readout circuit for SNSPDs. The nanowire acts as a switch which opens when the photon is absorbed, causing the bias current to be shunted into the readout amplifier.

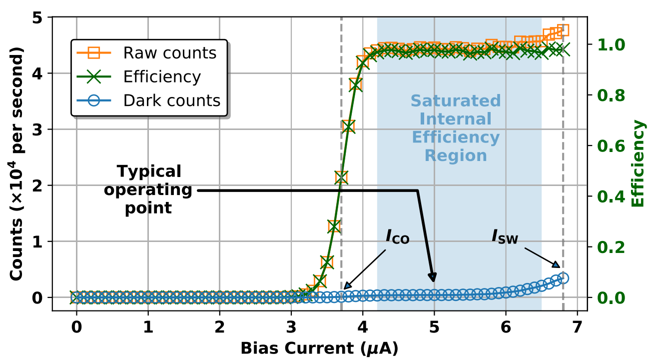

Fig. 4. Typical plot of system detection efficiency as a function of bias current.

the edge of the nanowire and subsequent dissipation contributes to hotspot growth [22], [23]. The hotspot grows until it covers the entire width of the nanowire, causing the resistance of the wire to increase to several kΩ on a time scale of picoseconds. To a first approximation, as illustrated in Fig. 3(b), the superconducting wire acts as a switch in parallel with a large resistance, which opens when the photon is absorbed. This pushes the current out of the nanowire and into the readout circuit, which is typically a 50 Ω amplifier. After the current is diverted, the nanowire cools off nearly instantly, returning to the superconducting state, and current rebuilds in the nanowire on time scales of 1–100 ns, depending on the device inductance. At this stage the device is ready to count another photon. Because the SNSPD intrinsically produces a digital pulse, it avoids the noise and instability associated with analog signal integration and readout.

Fig. 4 shows a typical plot of system detection efficiency (SDE) as a function of bias current for an SNSPD. As the bias current is increased, the detection efficiency also increases until it reaches a "plateau" region in which the efficiency is independent of bias current. When the current is greater than or equal to the switching current (I_{sw}), the nanowire switches from the superconducting to the non-superconducting (normal metal) state, and is no longer capable of detecting photons. Note also the cutoff current (I_{co}), which is the inflection point of the sigmoidal curve. The I_{co} can roughly be considered the current at which the nanowire begins detecting photons. Generally, I_{co} will be a function of the photon energy, with I_{co} being smaller for larger photon energies.

E. Principle Figures of Merit

Ideal single-photon detectors must show high performance in several figures of merit. These include, but are not limited to:

1) System detection efficiency (SDE)
2) Photon-number resolution (PNR)
3) Dark-count rate (DCR)
4) Recovery/reset time (or low dead time)
5) Timing jitter
6) Maximum count rate/response nonlinearity
7) Photon state sensitivity (polarization, bandwidth, etc.)
8) Scalability (multi-pixel arrays, low readout-circuit complexity, high operating temperature, etc.)

Different technologies possess varied advantages in each of these metrics. For example, TESs possess intrinsic photon-number resolution capability for up to double-digit photon numbers, but might suffer from high timing jitter and more complex readout electronics. Table I lists the performance records for some of the figures of merit for the various superconducting detector technologies mentioned above. Although we list the maximum number of distinguishable photons, as a comparison of photon-number resolving detectors, it is worth remarking that the maximum number of resolved photons and the system detection efficiency only are not sufficient to give a quantitative measure of photon-number resolution, or fidelity. The detector fidelity in resolving photon number is very important for quantum information and metrology applications. One such quantitative measure of the photon-number resolution representing the probability that the detector gives the correct photon number, was proposed in [24]. This measure could also be useful in directly comparing the efficacy of different detectors in resolving photon numbers as detector technologies continue to evolve.

As Table I illustrates, both TESs and SNSPDs show better record performances when compared to other technologies. It must be noted that multiple records are seldom shared by the same citation. High performance along one metric can require compromises in other metrics. For example, the SNSPD that reports a maximum count rate of 1.5×10^9 counts/s [25] can only operate at such count rates at an efficiency of 12%. Similarly, a low SNSPD timing-jitter value of 2.6 ps [26] was obtained for a narrow, straight segment of nanowire, which is not conducive to efficient coupling with optical modes. Table II shows the performance of the same devices cited in Table I for all the other metrics (where reported) for TESs and SNSPDs. Different applications can require high performance along different metrics, and can often tolerate mediocre performance along others. Hence, application-specific designs might not need to hit record values for every figure of merit. Nonetheless, joint high performance in multiple figures of merit has become a pressing goal in the field.

II. Present State-of-The-Art for TES and SNSPD

A. Efficiency

The record-high detection efficiencies in Table I are owed primarily to improvements in coupling guided optical modes to the absorptive active area. Fig. 5(a) shows a schematic, exploded diagram of a self-aligning fiber-coupled mounting package designed by Miller et al. [27] for both TESs and SNSPDs. The devices are fabricated in key-hole-shaped dies which fit snugly in standard 2.5 mm inner-diameter zirconia sleeves meant for fiber-to-fiber couplers. Such mounts, when used with ceramic-ferrule terminated single-mode fibers with AR-coated front faces, offer

TABLE II
DEVICE PROPERTIES FOR TESS AND SNSPDS LISTED IN TABLE I.

Device	Efficiency	Number resolution*	Recovery time§	Timing jitter	Dark counts	Max. count rate	Active area (μm^2)	Temperature
TES					counts/s	counts/s		T_c
W TES [19]	95 % (1556 nm)	7	800 ns	/	100	/	25 x 25	0.1 K
Ti TES [31]	98 % (850 nm)	7	100 ns [43]	30 ns [43]	/	10^5	10 x 10	0.3 K
Ti/Au TES [36]	< 4.1 % (1570 nm)¶	29	/	/	/	10^4	20 x 20	0.1 K
W TES [44]	/	4	760 ns	4 ns	/	10^5	/	0.1 K
W TES [37]	/	16	~ 2 μs	/	0.06	10^4	25 x 25	0.08 K
Ti/Au TES [41]	83 % (940 nm)	/	75 ns	74 ns‖	/	/	8 x 8	0.3 K
W TES [45]	23 % (1064 nm)	/	1.53 μs	/	0.0086	/	25 x 25	0.08 K
W TES [51]	/	5	460 ns	/	/	/	25 x 25	0.08 K
W TES [49]	9.7 % (850 nm)	/	60 μs	0.1 μs	/	10^4	~ 18 x 18 x 36 pixels	0.08 K
SNSPD							fill-factor in ()	operating T
MoSi SNSPD [32]	98 % (1550 nm)	≥ 1	~ 100 ns	/	500	10^5	~ 1900 (57 %)	0.75 K
NbN SNSPD [33]	98 % (1590 nm)**	≥ 1	42 ns	66 ps	100	2×10^7††	415 (54 %)	0.8 K
NbTiN SNSPD [34]	99.5 % (1350 nm)	≥ 1	33 ns	15 ps	300-500	3×10^5	50 (50 %)	2.5-2.8 K
NbN SNSPD [38]	5.6 % (1550 nm)	≥ 4	28.6 ns	16 ps	27	10^5	11 x 10 (50 %)	1.0 K
NbTiN SNSPD [40]	83 % (860 nm) [51]	≥ 6	> 25 ns‡‡	26 ps	< 1	10^6	15 x 15 (56 %)	0.5 K
MoSi SNSPD [39]	77 % (1550 nm) [52]	≥ 4	< 25 ns [52]	66 ps	< 10^4	5×10^7††	16 x 16 (42 %)	0.82 K
NbN SNSPD [42]	0.01 % (950 nm)	≥ 1	80 ps‡‡	16 ps	10	10^5	10 x 10 (60 %)	4.2 K
NbN SNSPD [26]	/	≥ 1	/	2.6 ps	/	/	0.12 x 5 (100 %)	0.9 K
NbN SNSPD [46]	10 % (1550 nm)	≥ 1	/	60 ps [54]	0.1	/	15 x 15 (50 %)	0.4 K
MoSi SNSPD [47]	84 % (370 nm)	≥ 1	90 ns	60 ps	0.01	/	~ 2500 (55 %)	4.2 K
NbN SNSPD [25]	72 % @ 10^7 counts/s	≥ 1§§	4.1 ns §§	~ 240 ps	< 10§§	1.5×10^9	~ 175 (45 %)	2.2 K
WSi SNSPD [50]	8 %	≥ 1§§	/	250 ps	110§§	10^7	960 x 960 (36 %)	0.73 K

*Maximum distinguishable photon number; R = E/ΔE is the spectral resolving power.
§$1/e$ decay time.
¶Inferred from efficiency of 20×20 μm^{2}device in same reference.
‖Only rise time reported.
**Over 95% across 1530–1630 nm.
††At half the maximal efficiency.
‡‡Inferred from figure.
§§Per pixel.

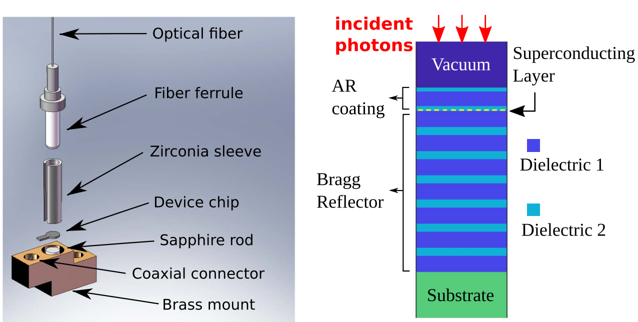

(a) (b)

Fig. 5. (a) Self-aligning fiber-coupled mounting package for nanofabricated optical detectors [27] (Image reproduced from [28]). (b) Typical vertical stack of the detector at the active area. The bottom reflector could also consist of a metallic mirror and a dielectric separator. A design could also include spacers around the active area to ensure fiber-to-top-surface separation.

a low-loss means of optically coupling to the detectors. The vertically-illuminated absorptive elements in the active area are further encased in a resonant optical stack composed of layers of metals and/or dielectrics, which are optimized to trap light at specific wavelength ranges to ensure multipass interactions with the absorber. These optical stacks in general consist of a reflective component below the active area, and an anti-reflection component above (Fig. 5(b)). The layer-thicknesses in all-dielectric Bragg-style reflectors below the superconducting layer can also be modulated to optimize absorption at multiple wavelengths of interest [29]. An alternative means of coupling optical modes to absorptive superconducting regions besides: self-aligning packages, direct freespace illumination, and waveguide integration, is evanescent coupling through microfibers [30]. This approach can offer ultra-wide bandwidths of operation (spanning from visible to near-IR), though it is yet to yield high-efficiency performance.

As demonstrated previously [55] and adopted by other superconducting technologies, TES detectors were optimized for high detection efficiency at specific wavelengths from near-ultraviolet to near-infrared by designing multilayer structures that enhance the absorption of light into the active device material. Using this technique, absorption in W TES has been increased from 30% in bare W film to above 95% for W embedded in an optical multilayer structure optimized for various target wavelengths from UV to near-IR [19], [56]. The same technique was adopted by other optical TESs using different superconducting detector materials: Ti [57], Ti/Au [58], Hf [59], as well as SNSPD devices as described in this paper.

Since TESs generally operate at sub-Kelvin temperatures, compatibility of various dielectric and metallic layers used in the optical stack design is very important, in order to avoid stresses that arise from the differences in coefficients of thermal expansion. This is particularly relevant for superconducting films with crystallographic structures susceptible to thermal-stress induced suppression of T_c, such as with W [60], or to transition broadening, which can result in a significant increase of TES recovery time [59].

One advantage of amorphous materials such as WSi and MoSi used in SNSPD device fabrication, is that they are not as susceptible to stress-induced superconducting transition changes compared to polycrystalline materials.

Like TESs, the efficiency of SNSPDs is also the product of the internal, coupling, and absorption efficiencies. The self-aligned coupling scheme and the vertical, layered stack of optimized thicknesses all contribute to maximizing the coupling and absorption efficiencies. The superconducting films in the active areas of SNSPDs typically require more multipass interactions than in TESs, due both to their sub-unity fill factor and their smaller thicknesses. Consequently, non-absorbing all-dielectric reflective structures at the bottom of the stack result in higher absorption efficiencies than partially-absorbing metallic mirrors [32], with the advantage waning for thicker nanowire films. The all-dielectric design causes a significant transverse divergence of the optical beam trapped within the optical stack prior to complete absorption, necessitating a wider active-area coverage resulting in increased kinetic inductance (causing increased jitter and recovery times) [61]. Usage of superconducting materials that show target-wavelength single-photon sensitivity at larger thicknesses can circumvent this constraint [34]. Using multiple layers of thin, superconducting nanowire meanders in a so-called SNAP (superconducting nanowire avalanche photon detector) configuration [33], [62] can increase single-pass absorptive thickness and curtail beam divergence. Multi-layer nanowire structures can also be optimized for wider contiguous bandwidths spanning $\sim$100 nm at near-IR wavelengths [33].

Internal efficiency in SNSPDs is the efficiency with which an absorbed photon results in an electrical output pulse. At low bias currents, SNSPDs are not sensitive to photon absorption. Higher bias currents increase the probability of hotspot formation via absorption of a photon of sufficient energy. When the internal efficiency is saturated, this results in a "plateau" of the efficiency as a function of the bias current (see Fig. 4). At the higher end of the saturated region close to switching current, the SNSPD "switches," i.e., gets stuck in a non-superconducting "normal" state when a detection-event occurs, requiring the bias current to be ramped down to zero and ramped back up again to resume detections. SNSPDs that do not see internal-efficiency saturation (for a given photon energy) before switching may have to be redesigned with narrower nanowire widths, thinner films, or reduced fill factors at the meander bends to limit local current crowding [61], [63]–[65].

SNSPDs are biased at currents within the internal-efficiency saturation region (Fig. 4) for high-efficiency operation. Higher bias-current operation can result in lower timing jitter due to an increased amplified-pulse voltage peak (for given amplifier and line noise), whereas lower bias currents help prevent accidental detector switching at high count rates in devices that are read out using AC-coupled RF amplifiers. Fiber-coupled SNSPDs have shown system-detection efficiencies exceeding 98% at near-IR telecom wavelengths [32]–[34].

B. Polarization Sensitivity

Polarization sensitivity (PS) is typically defined as the ratio of the maximum to the minimum system-detection efficiencies across all input polarization states of photons of a given wavelength. TESs are inherently insensitive to polarization for normally incident optical beams due to the cylindrical symmetry of the vertical stack within the optical-beam diameter. SNSPDs whose nanowire meander geometries consist of grating-like arrangements of parallel strips of nanowires in the active area show an innate polarization sensitivity. In general, the absorption efficiency is higher for TE-polarized light (electric field vector parallel to the nanowire) and smaller for TM-polarized light, though this can be reversed with clever AR-coating configurations. The difference between TE and TM absorption efficiency is generally on the order of 10–15%, but can be higher or lower depending on the geometry of the meandering wire. Reducing PS to near unity is desirable because applications which rely on high efficiency and high throughput [66]–[68] may otherwise need to introduce polarization controllers and other polarizing elements before directing light to the detectors, which adds complexity and can be a source of loss. Polarization-dependent efficiency also introduces a security vulnerability into phase-encoded quantum-key distribution methods [69].

PS can be made near-unity at single target wavelengths via clever engineering of top-dielectric-coating thicknesses in the vertical stack [70]. The standard approaches to reducing PS over broader bandwidths have resorted to introduction of discrete rotational symmetries in the meander geometry. This has been done, for example, by stacking two layers of meanders with perpendicular orientations within the stack [62], which resulted in a PS of 1.02 with an SDE value of 87.7%. Alternatively, the meander layout can utilize space-filling 1-D fractals such as Sierpinski or Hilbert curves; this was shown to yield a PS of 1.02 with 91% SDE [71]. The challenge for efficient detection with fractal meanders stems from the introduction of bends in the active area, which have a hard time reaching internal-efficiency saturation due to current crowding at the inner radii [61], [63]–[65]. Yet another solution is the use of spirally-patterned meanders [72], which have achieved a PS of 1.03 at 92.2% SDE for 1550 nm light. The efficiency of spiral meanders is limited by a low-fill-factor central region, in addition to the introduction of bends in the active area.

Recent advances in SNSPDs have shown that micrometer-wide superconducting thin-film strips can be sensitive to near-IR single photons [73]–[78]. Such micrometers-wide wires, or 'microwires' are 2–3 nm thick, which is thinner than is typical for nanowires. This technology has enabled high-fill-factor meanders in excess of 0.9 in the active area with reduced preponderance of superconducting material close to the edges, which is responsible for the innate polarization sensitivity of traditional meander geometries in SNSPDs. Microwires in conjunction with a novel candelabra-style meander (see Fig. 6) [61], [65] that decouples the switching current with active-area fill factor, have achieved a PS of 1.02 with SDEs of 96% at count rates of 10^5 counts/s [61].

C. Recovery Time

The recovery rate of the optical TES is limited by the weak thermal link between the electron and phonon systems. While a weak thermal link is required so that a photon can be converted to a detectable electrical signal, the weakness of this link can lead to long recovery times compared to other single-photon detectors such as SNSPDs (see Table I).

It is important to note that during the thermal recovery time, the TES is still able to receive and detect a photon, and therefore it

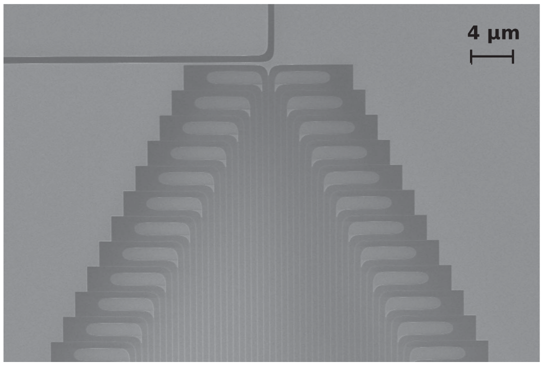

Fig. 6. An SEM image of a candelabra meander microwire pattern [61] etched into WSi, showcasing a high fill-factor of 0.91 in the active area and a low local fill-factor of 0.33 at the hairpin bends outside of the active area.

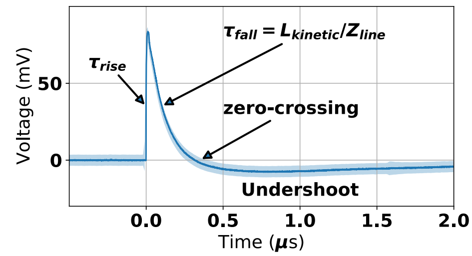

Fig. 7. Detection pulse from an large-area SNSPD with kinetic inductance $L_{\text{kinetic}} = 5$ uH, amplified using two-stage room-temperature RF amplifiers with a net gain of 38 dB below 500 MHz. The impedance of the readout line was $Z_{\text{line}} = 50\ \Omega$. Note the zero-crossing and the undershoot of the voltage trace into the negative region that persists for microseconds due to discharge from the input capacitance of the AC-coupled amplifier circuit.

has no dead time, which is unique among photon counting detectors. However, if an absorption event occurs during the recovery of the detector, signal pile-up may occur and requires complicated post-processing of the detector response. Consequently, short recovery times of TES devices are needed for enabling high-repetition rate experiments. Decreasing the recovery time for optical TES detectors is an active area of research and the following will describe two ways of achieving this.

The response time of the TES in an electron-phonon decoupling limit is inversely proportional to the cube of the operating temperature, and independent of the sensor volume. When voltage biased, the TES response is significantly sped up due to negative electrothermal feedback: $\tau_{\text{etf}} = \tau/(1 + \alpha/n)$, $\tau = C/G$ [15]. Since the TES heat capacity is $C = \gamma VT$, where γ is the specific electron heat capacity coefficient, and the thermal conductance to the bath is $G = n\Sigma_{e-p}VT^{n-1}$, where Σ_{e-p} is the electron-phonon coupling constant limiting the heat flow to the substrate and $n \sim 5$ is the power-law dependence of the thermal conductance between the superconducting film and the heat sink; the TES recovery time can be written as $\tau_{\text{etf}} = (\gamma/n\Sigma_{e-p}T^{n-2})/(1 + \alpha/n) \sim T^{-3}$.

Based on the inverse dependence on the cube of the operating temperature, using superconducting thin film materials with high T_c or tuning the transition temperature of a specific material or bilayer to a desired high T_c can significantly speed up the recovery of a TES detector. For example, Kobayashi et al. [41] have used Ti/Au bilayer as the TES superconductor material, with a T_c of 314 mK which resulted in a recovery time constant of 74 ns, with energy resolution of 0.42 eV (FWHM) at 940 nm wavelength.

Another way of speeding up TES devices is the use of a faster alternative heat dissipation path. Calkins *et al.*, have shown that by adding Au pads on top of W TES devices, the device recovery time reduced to 460 ns, showing an improvement of a factor of 4 over devices with no Au pads, without affecting energy resolution [51]. Since the thermal electron-phonon coupling parameter of gold Σ_{Au} is $\approx 10\times$ larger than for tungsten, one can engineer the thermal coupling by adding a controlled volume of gold to the TES. Since the Au-e^- system is strongly coupled to the W-e^- system, a strong thermal link between the Au-e^- and phonon systems allows for faster thermalization to the thermal bath, modifying the thermal coupling constant of the whole system. Ultimately, the inductance in the TES readout circuit and the SQUID amplifier bandwidth will limit the TES rise time and recovery time.

SNSPDs are significantly faster than TESs, which makes them particularly attractive for many quantum optics applications. Both the rise and recovery times of SNSPDs are entirely dependent on the kinetic inductance of the meanders and the input/line-impedance of the readout method. The kinetic inductance is merely the product of the sheet inductance of the superconducting film (expressed in H per square) and the aspect ratio of the current-carrying path in the meander. Note that the gross geometry of the nanowire makes a negligible contribution to total inductance at these length scales. Thick ($\sim$10 nm) superconducting films used for SNSPDs are typically made of polycrystalline materials like niobium nitride (NbN) or niobium-titanium nitride (NbTiN), possessing sheet-inductance values of 50–100 pH per square. Thinner ($\sim$2–5 nm) amorphous superconducting films like MoSi or WSi boast sheet inductance values of 150–300 pH/sq. Meanders in thinner films would also be required to cover a larger active area in vertically illuminated stacks to compensate for beam divergence, which further increases the net kinetic inductance in high-efficiency devices.

The rise time of SNSPD detection pulses (τ_{rise}) in simple readout schemes is, to first order, the ratio of the kinetic inductance (L_{kinetic}) and the resistance of the hotspot. The pulse then decays exponentially with a time constant ($\tau_{\text{fall}} = L_{\text{kinetic}}/Z_{\text{line}}$), where Z_{line} is the input-impedance of the readout circuitry. In the simplest method of readout, this is simply the line impedance of the coaxial line (50 Ω). A typical detection pulse read out of a coaxial line using room-temperature RF amplifiers is shown in Fig. 7.

Recovery times can be improved by increasing the readout line impedance using Π- or T-networks of passive resistors [32], [61] but these approaches seem to limit maximum sustainable count rates. Alternatively, a radical change in the meander geometry which can provide multiple parallel current paths through nanowires covering the active area can drastically reduce the kinetic inductance. N identical parallel sub-meanders with nanowire widths matching a single full-coverage meander boast a kinetic inductance that is smaller by a factor of N^2.

This SNAP configuration was used in [42] with $N = 12$ to achieve a recovery time of 80 ps. SNAP meanders have to be carefully designed to ensure that a hotspot in one branch triggers a cascading hotspot generation in all branches.

The above record was achieved in epitaxially grown NbN nanowires, and cannot be replicated with sputtered amorphous, or even polycrystalline superconducting films. This is because besides the electronic recovery time, there is another timescale associated with the thermal relaxation of the hotspot, which imposes a lower limit. For amorphous films like MoSi and WSi, this is typically 10–20 ns for the usual cross-sections. For polycrystalline sputtered films like NbTiN, this can be as low as 3 ns. Due to detector nonlinearities and pulse pile-up effects, the effective detection efficiency suffers with increased count rates [61], with the trade-off being worse in slow-recovery detectors.

D. Timing Jitter

In addition to faster recovery times, low timing jitter is another desirable parameter for most single-photon experiments [79]. The timing jitter is the uncertainty in identifying the arrival time of the photon.

For any timing pulse signal, the jitter or timing uncertainty for crossing a threshold is determined by the noise and the underlying slope of the signal at the point of crossing:

$$\Delta t_\sigma = \frac{\sigma}{dA/dt|_t} \approx \frac{\sigma}{A_{\max}} \tau_{\text{rise}}, \tag{1}$$

where σ is the root-mean-square (RMS) noise of the electrical signal, dA/dt is the slope of the signal at a given time t, τ_{rise} is the rise time and A_{max} is the maximum amplitude.

For TES, the absorption of a photon gives rise to a current signal characterized by an RMS (root mean square) noise and amplitude corresponding to a certain timing jitter. Assuming that the noise contribution from the SQUID readout is sufficiently low, the main contributions to the noise in the TES signal are a combination of Johnson noise in the device and thermal fluctuations between the device and the bath [15]. The rise time of the electrical signal for TESs is generally limited by the overall inductance in the readout circuit and the resistance of the TES, as well as the bandwidth of the external amplifier. Any jitter related to the position of photon absorption is generally negligible for TES detectors.

Using a SQUID chip designed to have lower input inductance ($L = 24$ nH) as well as using low overall inductance of readout circuit in addition to high-bandwidth room-temperature amplification, Lamas-Linares et al. have demonstrated timing jitter FWHM values of 4.1 ns for 1550 nm single photons and 2.3 ns for 775 nm [44] in W TES devices, without significant degradation of the device energy resolution (0.33 ± 0.02 eV). The lower timing jitter for higher energy photons is due to higher amplitude of the TES output waveform.

For SNSPDs, there are three contributing factors to jitter: amplifier noise, geometric jitter, and intrinsic jitter. Amplifier noise for SNSPDs is also described by Equation (1) above. Amplifier noise can be minimized through the use of cryogenic amplifiers located either at 40 K or 4 K stage of the cryostat. The second contribution to jitter is geometric jitter. The nanowire acts as a microwave transmission line, resulting in small variations in the arrival time of the pulse at the counter based on the precise location on the meandering wire where the photon is absorbed. The sub-3 ps record-low jitter from Table I [26] was measured in a single 5 μm long nanowire strip to minimize geometric effects. Geometric jitter can also be eliminated using differential or double-ended readout [80]. The final contribution to jitter is intrinsic jitter, and results from statistical variations in the time it takes for the hotspot to form. Intrinsic jitter varies with photon energy and the material used to fabricate the nanowire, and depends critically on the physics of the hotspot formation process. Fano fluctuations in the number of Cooper pairs broken [81], transverse-position-dependent delays in hotspot formation [82], [83], as well as inhomogeneity in film properties such as thickness or granularity [84] have all been theorized as contributors to intrinsic jitter [85]–[88].

E. Maximum Count Rate and Nonlinear Response

As illustrated in Tables I and II, TES devices with counting rates of 10^5 counts/s and photon-number resolution of 7 at 1550 nm have been demonstrated. In order to achieve the fastest counting rate of a TES detector, the readout circuit inductance needs to be minimized. In addition, design constraints for stabilizing the TES detector against electrothermal oscillations that can develop in the dynamic solutions to the coupled heat flow and electrical circuit equations (corresponding to a transfer of energy back and forth from the inductor to the TES thermal heat capacity) need to be addressed [89].

Recently, it has been shown that photon numbers can be efficiently measured in real time using a custom hardware processor to process TES pulses on the fly at a count rate of 10^4 counts/s [37]. Up to 16 photons achieving up to part-per-billion discrimination for low photon numbers were measured on the fly using this method.

The maximum count rates reported for SNSPDs are those which are demonstrably sustainable without the device switching into an insensitive, "normal" state. The bias current in the photosensitive nanowire meander will be reduced to below the setpoint immediately following a detection, and will take time τ_{fall} to recover. Meaning that even when the bias-current setpoint is operating at saturated internal efficiency, the device will not efficiently detect photons arriving too soon after a detection event. As a rule of thumb, two separate detection events have to occur $3\tau_{\text{fall}}$ apart for their detector responses to have been independent. As a consequence, the detection efficiency of a single meandering current path in the active area is dependent on the incident photon rate [61]. The record maximum SNSPD count rate [25] of 1.5 Gcounts/s was achieved using multiple interleaved meanders in the active area and combining their RF pulses into a single line to be amplified. A similar effect can be mimicked using a SNAP-style arrangement wherein, unlike in typical SNAP detectors, the independent meanders are biased at a low current to prevent the cascading avalanche of hotspot generations [53]. So when a single meander detects a photon, the other meanders serve as buffers for the DC and low-frequency components of the bias current, and remain photosensitive during the initial-meander recovery.

Another significant source of detector nonlinearity can occur due to non-resistive input-impedance (from the device's viewpoint) of the readout circuit. When the detection pulses are read out of SNSPDs using AC-coupled RF amplifiers, their voltage trace will show a zero-crossing and an undershoot region after detection which can persist for several microseconds (see Fig. 7). This is due to the input capacitance of the amplifier chain getting charged up during the initial positive lobe and then slowly discharging by driving excess current back into the device. The amount of undershoot is proportional to the input capacitance of the amplifier system, which is monotonically related to the low-end frequency of the amplifier's gain bandwidth. The voltage trace of the pulse closely resembles the inverse plot of the amount of current in the SNSPD meander. Meaning that the detector's bias current after a detection event (in the undershoot region) is slightly higher than the DC setpoint, briefly making the detector more sensitive to photons and increasing the probability of switching upon rapid successive detection events. This undershoot can be avoided by using DC-coupled amplifiers, as is usually done in cryogenic amplifier systems. More sophisticated readout schemes, such as active-quenching circuits [90] can also prevent the undershoot but will obscure the state of the current in the detector from easy measurement. DC-coupled cryogenic amplifiers are necessary to ensure that the devices see purely resistive impedance across a wide bandwidth in the readout circuit [91]–[93].

F. Photon-Number Resolution

Based on its microcalorimetric principle of operation, the optical TES generates an output signal that is proportional to the cumulative energy in a photon absorption event. This proportional pulse-height enables the determination of the energy absorbed by the TES and the direct conversion of sensor pulse-height into photon number. The ability to discriminate between photon numbers is determined by the energy resolution of the TES and the incident photon energy. The fundamental energy resolution is given by [89]: $\Delta E_{\mathrm{FWHM}} = 2.355\sqrt{4k_{\mathrm{B}}T_e^2 C\sqrt{n/2}}/\alpha$, where $T_e \sim T_c$. Lower values of T_c improve the energy resolution of the TES. However it also slows down the device recovery, since the recovery time scales with $\sim T^{-3}$.

In some applications, it is important to be able to count photons at high incident power. The ability to discriminate higher photon numbers is related to the TES linearity, or the saturation energy of the TES. Above a certain energy, $E_{\mathrm{sat}} \sim T_c C/\alpha$, the superconducting film is driven to its normal state and loses its ability to discriminate photon numbers, becoming a 'click/no-click' detector. There is a trade-off between high E_{sat} and energy resolution, so different applications might have to prioritize one over the other.

Fig. 8(a) illustrates the photon-number-resolving capability of the TES. The TES was illuminated with weak coherent state pulses with a mean photon number per pulse of 2 at 800 nm wavelength. Also visible is a 2 μm wavelength blackbody photon

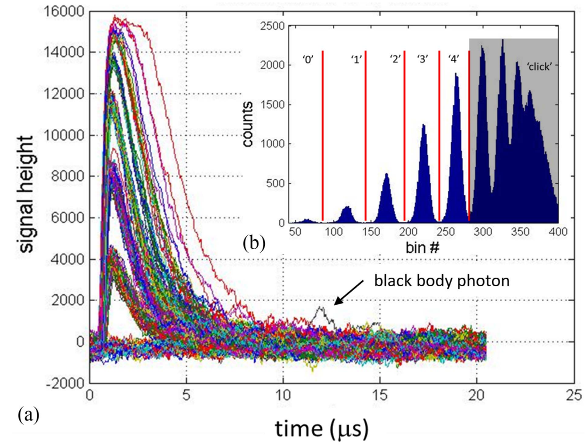

Fig. 8. Many TES output waveforms from 800 nm incident photons. The pulse heights correspond to energy deposited. Inset shows pulse-height binning for photon-number discrimination. Figure reproduced from [56].

detection at about 10 μs after the weak coherent pulses. When TESs are coupled to typical telecom optical fibers, background photons such as this result from the section of the high-energy tail of the room-temperature blackbody emission spectrum that falls below the long cutoff wavelength of the fiber around 2 μm [94] or can be due to spurious visible wavelength photons coupled to the detector from the lab environment or even high energy cosmic ray muons absorbed in the detector chip. When the energy of the signal photons is large enough, the blackbody photons can easily be separated out by pulse height analysis. As can be seen in Fig. 8(a), at higher photon numbers (>4), the TES response enters the nonlinear regime close to the normal conducting regime, and the photon-number resolution capability degrades.

Post-processing of the TES output waveforms is commonly done to maximize the signal to noise ratio. One fast, reliable method is optimum filtering using a Wiener filter [95]. This method yields a projection of each waveform onto a known template, resulting in an outcome that is approximately proportional to the absorbed energy, hence the number of photons for a given absorption event. An example is shown in Fig. 8(b) displaying the pulse-height histogram for a measured coherent state with mean photon number of ≈ 5. Since the optimum filter relies on a known linearly-scalable detector response, the method fails when the assumed detector response does not match the actual response, i.e. when entering the non-linear region. This effect is evidenced by the reduced visibility of the pulse height peaks for photon numbers larger than 4. To improve the photon-number resolution at higher photon numbers in the non-linear region, one can find the most optimum representation of each photon-number response [96]. A few other methods have been proposed to extend the photon number resolution close to the normal-conducting region [97] as well as far beyond the normal conducting region [98].

Recently, a lot of research has been dedicated to investigating SNSPD's ability to discriminate photon numbers. The electronic traces of the detection pulses from SNSPDs contain information about the total resistance of all of the hotspots generated within a small (10–100 ps) temporal window. Under monochromatic or narrow-bandwidth optical-input-state conditions, all the hotspots generated in the active area (with constant nanowire width) will have nearly-identical resistances (typically 1–10 kΩ, depending on the nanowire material, geometry, and photon energy). Therefore, the electronic traces can be used to count the number of hotspots generated, which gives SNSPDs limited number resolution for up to 3-6 photons [40], [99], [100]. This information is usually contained in the slope of the rising edge of the detection pulses, and can only be extracted with low-noise (typically cryogenic) electronic amplification. Alternatively, an impedance-matching taper can be fabricated into the superconducting film, wherein a lengthy microstrip of slowly tapering width is used in the readout circuit to match the (single) hotspot resistance to the 50 Ω coaxial-line impedance. This can increase the signal-to-noise ratio in the traces, and the voltage peaks or pulse heights will correspond to the number of simultaneously generated hotspots [38], [101]. Impedance-matching tapers can introduce a higher kinetic inductance as well as frequency-dependent reflections, resulting in long, distorted readout pulses which can limit the maximum count rate. The advent of microwire technology could allow for geometries which host hotspots with resistances close to 50 Ω, which would obviate the need for tapered readouts while retaining the lumped-element character of the device.

The mechanism of RF pulse extraction from the active area is substantially influenced by the impedance mismatch between the hotspots and the readout line [102]. Thus, the number-resolving ability decreases at higher numbers, limiting SNSPDs to values well below the TES records. Furthermore, SNSPDs are not sensitive to photon absorption immediately after a hotspot-generating detection event due to all of the bias-current having "exited" the device. For photon-number resolution, all of the hotpots need to be created within a small temporal window of size 10–100 ps, a condition that is orders-of-magnitude stricter than for TESs. SNSPD detector-tomography efforts have yet to measure this aspect of these detectors. Photon-number resolving SNSPDs will most likely be limited to applications with ultrafast optical pulses and requirements limited to discriminating between single- and multi-photon detections, such as rejection of higher-order terms in squeezed-vacuum photon-pair sources [66], [100].

Several experiments have been performed recently by various research groups around the world in using SNSPD arrays for photon-number-resolved measurements [25], [103]. This approach relies on splitting the optical mode amongst a large number of detector elements or pixels. However, it is ultimately limited in fidelity due to either the limited signal-to-noise ratio of the output pulses or non-unity detection efficiency of the array. For array-style detectors that split the optical mode equally across M non-number-resolving pixels, the probability of undercounting N simultaneously-incident photons is $1 - ({}^{M}\mathrm{P}_{N})\eta_1^N/M^N$, where η_1 is the overall single-photon SDE. Even with $\eta_1 = 1$, an 10-pixel array undercounts $N = 2$ photons 10% of the time. One would need a 100 pixels to reduce that to 1% [104]. Increasing number of pixels introduces complexity to the array readout, which in most designs decreases the inter-pixel fill factor, thus further reducing η_1.

G. Dark-Count Rate

When discussing dark counts for SNSPDs and TESs, one must differentiate between background counts and intrinsic dark counts. Background counts are counts due to background photons, which generally originate from blackbody radiation but can also be due to stray high energy particles such as cosmic rays. Background counts can be reduced significantly when working at telecom wavelengths by coiling the fiber close to the device in a tight coil with radius $\sim$1 cm. The bend loss for long wavelength photons will be higher than for the signal of interest. The record-low dark-counts in Table 1 were achieved by addressing long-wavelength radiation. Shibata et al. [46] obtained a dark count rate of 0.1 counts per second by introducing cold-filters in front of the fiber to block guided blackbody radiation. The UV-sensitive WSi SNSPDs fabricated by Wollman et al. [47] were thicker (10 nm) than is typical for that material, rendering them inherently insensitive to lower-energy photons and showing dark-count rates of 0.01 counts per second. Tight (low-radius) hairpin bends in the meander geometry have been shown to increase the intrinsic dark count rate due to the current-crowding effect at the inner radii [63]. Intrinsic dark counts in SNSPDs are counts which will be observed even in a perfectly shielded environment, and are generally due to statistical thermal fluctuations. At low bias currents, shielded SNSPDs have measured 4–5 counts in 180 hours of continuous operation [105]. Intrinsic dark counts increase exponentially as the bias current approaches the switching current.

Due to their almost zero intrinsic dark counts and background limited, TES detectors are also a key enabling technology in the search for Dark Matter. The Any Light Particle Search (ALPS II) experiment relies on TES detectors to detect the 1064 nm photons produced due to the creation and annihilation of an axion in the 'light shining through the wall' experiment [45]. The TES detectors have $> 90\%$ detection efficiency over 800 nm–1600 nm wavelength range. Intrinsic dark count rates of 1×10^{-4} s^{-1} were measured with no optical fiber attached to the TES, and a dark count rate of 8.6×10^{-3} s^{-1} with optical fiber coupled to the TES and with the other fiber end at 300 K. The main dark-count contribution for the fiber-coupled TES were due to blackbody photons from 300 K blackbody spectrum, so cooling the end of the fiber at 300 K and/or using a cold filter that reflects low energetic photons (as in [46]) should lower the dark counts rate further.

H. Array Readout

Array readout for SNSPDs is in an early stage of development. Only recently has SNSPD yield been improved to a degree which allowed the fabrication of large scale arrays, due in large part to the development and use of amorphous superconductors such as WSi and MoSi, which have excellent uniformity over large areas and can be deposited on a wide range of substrates.

The simplest form of array readout is direct readout, in which each SNSPD in the array has a dedicated readout line. The advantage of this simple technique is that the maximum count rate of the arrays increases linearly with the number of pixels. The primary disadvantage is that each readout line carries a heat

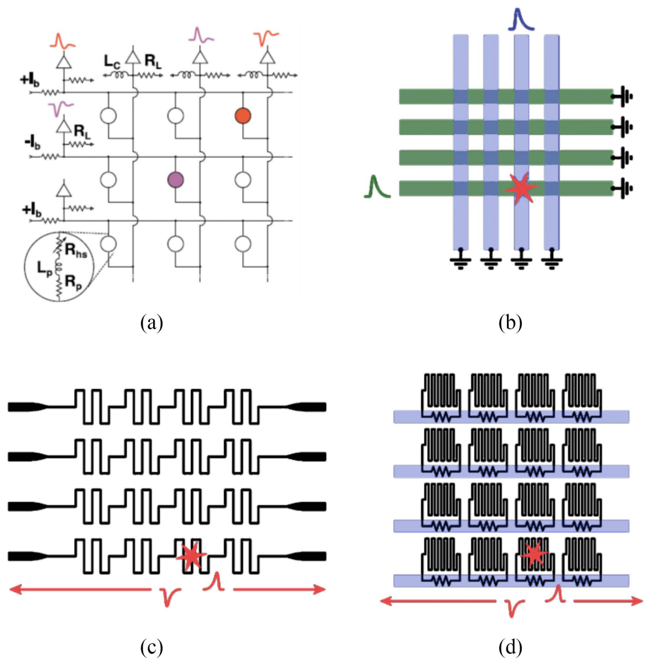

Fig. 9. (a) Row-column readout (b) thermal row-column (c) time-of-flight imager and (d) thermally-coupled imager.

load to the lowest temperature stage of the cryostat, which may increase the base temperature or result in a shorter measurement window before which a recycling or regeneration of the cryogenic system is required.

In order to mitigate the heat load problem, several multiplexing schemes are currently being explored. The most mature technique is known as row-column multiplexing, shown in Fig. 9(a). This scheme allows the multiplexing of N^2 pixels on 2 N readout lines. Each row contains N pixels wired electrically in parallel. The current flowing through each pixel in a given row then flows out through a unique column. Each row and column has an associated readout amplifier. When a detection event occurs in a pixel, the current is diverted out into a row amplifier. There is a simultaneous reduction in the current flowing through the column, leading to a negative pulse in the column amplifier. Correlations between positive row and negative column pulses are then used to determine the pixel which detected the photon. Row-column has been used to successfully multiplex up to 1024 pixels in a 32 $\times$ 32 array [50].

One disadvantage of the row-column scheme is leakage current to other pixels in a row when a detection event occurs. Not all of the current is shunted to the amplifier. This can be a problem for SNSPDs with low switching current, such as those used for detecting mid-infrared photons. The degradation of signal-to-noise ratio resulting from leakage current can make the row-column scheme unusable. Fig. 9(b) shows an alternative in which correlations between rows and columns are achieved through thermal interaction between the row and column pixels. Pixels in the rows and columns are wired in series instead of in parallel, eliminating the problems associated with leakage current [106].

Fig. 9(c) illustrates the time-of-flight multiplexing scheme. This scheme utilizes the transmission line nature of the nanowire and the relatively slow propagation velocity of an electrical pulse along the length of the nanowire (roughly $0.01c$, where c is the speed of light) to give spatial resolution. Each detection event produces a positive and negative electrical pulse which travel in opposite directions along the length of the nanowire. The difference in time of arrival between the pulses at the two ends of the nanowire can be used to determine the spatial location of the detection event. This is a very efficient method of multiplexing in that it drastically reduces the number of required readout lines for a given number of pixels. However, this technique also drastically reduces the maximum count rate of the array.

Fig. 9(d) illustrates another multiplexing technique known as the thermally-coupled imager. This technique utilizes the same time-of-flight scheme as shown in Fig. 9(c). However, in this case when an SNSPD detects a photon, the electrical pulse is sent to a resistive heater. The generated heat is coupled to a superconducting readout bus which lies underneath the resistor, separated by a thin dielectric. The heat generated by the resistor is large enough to generate a hotspot in the readout bus, generating pulses of opposite polarity which travel along the bus in opposite directions. This scheme is more scalable than that of the simpler time-of-flight imager. The pixels in each row are electrically biased in parallel, so that a fabrication defect in one pixel does not limit the operation of the rest of the pixels in the same row. Furthermore there is minimal leakage current between pixels in a row. Finally, the maximum count rate of the readout bus is independent of the number of pixels thermally coupled to it. This approach recently demonstrated a 1 kilopixel array [107], and has the most promise of achieving 1 megapixel in the near future.

Frequency domain multiplexing is also being explored, which is similar to the multiplexing scheme used with MKID detectors. This scheme is still in the early stages of development for SNSPDs [108].

Finally, readout of SNSPD arrays using single-flux-quantum circuits has been developed for arrays up to 64 pixels [109].

Regarding TES detectors for optical and near-IR applications, the focus in recent years has been on single pixel TES optimization, in contrast to the submillimeter astronomy applications that utilize kilo-pixel size TES arrays. As a result, more modest size arrays for astronomy and photon-counting microscopy applications have been achieved so far, such as arrays of sizes 6 $\times$ 6 [49] and 3 $\times$ 3 [110] pixels, respectively.

III. Application Specific Design

A. Quantum-Certified Random Number Generation

The high-purity polarization-entangled photon-pair source, routing optics, and detection setup used in the loophole-free Bell violation experiment [66] can be repurposed for certifiable, device-independent randomness generation [68]. All loophole-free Bell tests involve a couple of space-like separated measurement stations (name Alice and Bob by convention), a source of entangled particle pairs such as a laser-pumped spontaneous parametric down-conversion (SPDC) based setup, and a means

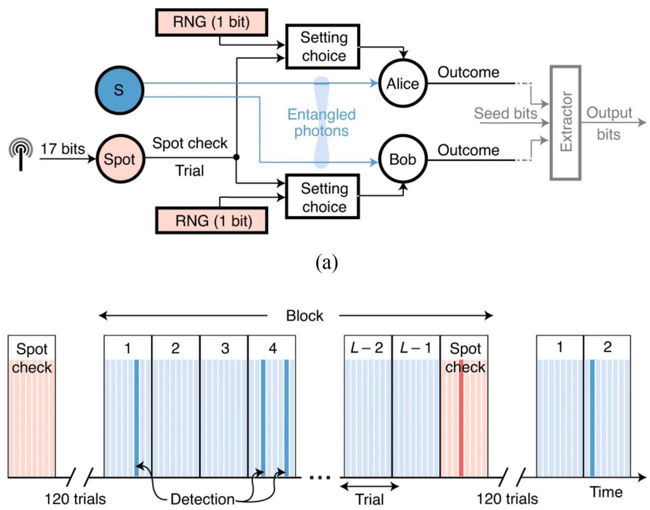

Fig. 10. Experimental setup for certified random-number generation. The source S sends entangled photons to space-like separated stations Alice and Bob. At the same station, 'Spot' randomly signals when to commit a spot-checking trial by using a 17-bit random number L, which is the size of a "block" of "trials". A single "trial" spans eight laser pulses pumping the photon-pair source. Alice and Bob only change measurement settings during a spot-check. A block (always ending with a spot check) consumes 17+2 random bits, and has a statistical probability of generating more than 17+2 bits on average, depending on the pair generation rate and system efficiency. The Bell-violation across an ensemble of spot-checks certifies the newly generated randomness with a confidence level that increases with the number of total blocks consumed in the process. Image reproduced from [68].

of distributing the pairs to Alice and Bob, such as a fiber network. The act of measuring for Bell violations requires both Alice and Bob to make random independent choices of measurement basis (typically between two settings) for every trial. These trials, therefore, consume random bits. The measurement outcomes, however, have randomness even when conditioned on additional or "side-channel" information.

In order to ensure that the setup generates more randomness than it consumes, NIST developed a protocol wherein Alice and Bob only rarely, but randomly, perform a "spot-checking" Bell trial. The data is now divided into blocks, which are composed of a variable number of trails between 1 and 2^{17}. Each block ends with a "spot-check" Bell-test trial where two bits of randomness are consumed from a classical source to make measurement choices. But the measurement settings are untouched throughout the rest of the block. A trusted third party, 'Spot,' uses a classical source of 17-bits of randomness to decide when a spot-check should occur, and neither Alice nor Bob (nor the source) can know in advance when a spot-checking trial can occur, or what the setting choices will be (see Fig. 10). Since an ensemble of Bell-violating spot-checking trials are required to certify the randomness generated, a desired confidence level is predetermined and sufficient blocks of data are gathered to ensure that the level is satisfied.

The experiment in [68] used 93% efficient SNSPDs, which brought their total system efficiency for pair detection (including all the coupling losses) to 76%. The pump laser at the source had a pulse-rate of 79.6 MHz. At the photon-pair rate used, 91 hours of data had to be gathered to generate around 2×10^8 bits of certified randomness at the desired confidence level. With the newer 98% efficient SNSPDs, the total system pair-detection efficiency has been brought up to 86%, allowing for each block to be 50–100× shorter, and enabling the same result to have been produced in under an hour of data collection.

In addition, the photon pair rate is kept low for two reasons: (a) avoid SNSPD nonlinearity for successive detections, and (b) limit double-pair generation, which can be a significant source of noise. Advances in polycrystalline sputtered films enables fabrication of SNSPDs that can fully recover saturation in internal efficiency within the pump laser's successive-pulse interval. Innate low-number PNR has already been shown to be useful in detecting and rejecting higher-order pair terms from squeezed-vacuum states [100]. Photosensitive microwires [73]–[78] can help reduce hotspot resistances to near 50 Ω, matching the readout line impedances [38], [101], further enhancing PNR ability. This, along with SNAP-like meander configurations [53] can herald the next-generation of high-efficiency, fast-recovery, PNR-capable SNSPDs which will move quantum-certified random-number generation from the proof-of-concept stage into the practical realm. Hitting record performance in multiple metrics will also help with more elaborate experiments involving multiple pair sources and greater-than-two coincident detection requirements.

B. Ion Traps With Integrated SNSPDs

Ion-based quantum computing is one of the most promising approaches due to the long coherence times demonstrated by ion qubits. One of the biggest challenges facing this approach, however, is scalability. Readout of the qubit state is typically performed using resonant fluorescence with a high-NA lens and photomultiplier tube (PMT). The use of bulky optical components and detectors is one of the limitations of scalability to a large number of ions. A more practical approach is the use of integrated detectors located on the trap itself. SNSPDs are a natural detector technology to use with ion traps, because they have demonstrated efficiencies above 85% in the ultraviolet (compared with ~30% from a PMT) [47], have ultra-low dark count rates, high maximum count rates, and 4 K operating temperature. Although ion traps do not require cryogenic temperatures, their performance is generally improved at low temperature.

Fig. 11 shows a linear RF surface electrode trap with integrated SNSPD designed to trap $^9Be^+$ ions [111]. The pink RF electrodes provide confinement transverse to the trap axis indicated by the black arrow. The surrounding segmented electrodes confine the ion at adjustable positions along the trap axis, from directly over the SNSPD (zone D) to zone A, 264 μm away from the SNSPD center. The ion is held ~39 μm above the surface of the electrodes, and hops to a smaller height of ~29 μm when directly over the SNSPD. The SNSPD is fabricated from 10 nm-thick $Mo_{0.75}Si_{0.25}$ with a superconducting transition temperature of 5.2 K. MoSi was chosen for this application because the operating temperature of the trap is 3.5 K, and the transition temperature of MoSi is generally higher than that of WSi. In principle other materials with high Tc could be used

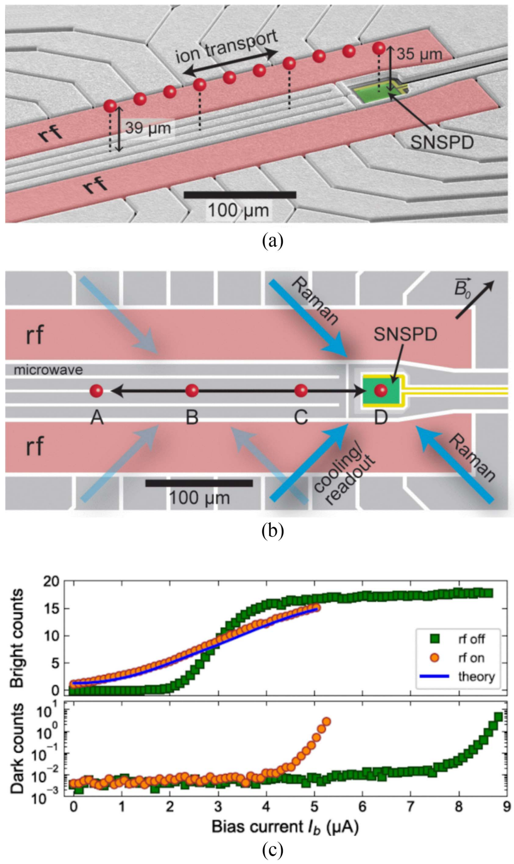

Fig. 11. (a) Trap configuration. (a) False-color scanning electron micrograph of the ion trap showing the rf electrodes (pink), SNSPD (green), and SNSPD bias leads (yellow). A trapped ion (red sphere, shown in multiple positions along the RF null line) can be transported along the trap axis by applying appropriate time-varying potentials to the outer segmented electrodes (grey). (b) Top view scale diagram showing four labeled trapping zones A-D along the trap axis (double-headed black arrow), as well as the geometry of the laser beams (blue solid arrows, here shown directed at zone D) and quantization magnetic field, which all lie in the plane of the trap at 45° angles to the trap axis. The laser beams can be translated horizontally to follow the ion as it is transported between zones, as indicated by the faint laser beam arrows directed at zone B. (c) Bright (top) and dark (bottom) counts in a 200 μs detection window versus SNSPD bias current, with trap RF either off (green squares) or on (orange circles). The blue line is a fit to a theoretical model simulating induced RF currents in the SNSPD.

such as NbN or NbTiN, and experiments with these materials are ongoing. Amorphous materials are generally more robust to processing and type of substrate compared to polycrystalline materials, which is one of the reasons MoSi was chosen.

The active area of the SNSPD was 22 μm $\times$ 20 μm. This gives an effective NA of 0.32 for the SNSPD, resulting in $\sim$2% of the fluorescence emitted by the ion being collected by the SNSPD. Knowledge of the excited state lifetime (8.850 ns) gives the photon flux emitted by the ion, which when combined with the ion-detector geometry can be used to estimate the photon flux incident on the detector. Comparing this incident flux to the SNSPD count rate gives an estimate of the SNSPD efficiency of 65%, significantly higher than the efficiency of a typical PMT.

Important considerations for this integrated device are the effect of the trap RF field on the performance of the SNSPD, and the motional heating of the ion caused by the RF field around the detector when it detects a photon. Due to the close proximity of the ion to the detector and the detector to the RF electrodes, both of these interactions are non-negligible. The RF field of the trap electrodes results in an induced current in the SNSPD at the RF frequency. Fig. 11(c) shows the bright counts and dark counts with the trap RF off and on. The result of the RF is a reduction in the DC switching current of the SNSPD from 8.9 μA to $\sim$5.3 μA. In addition, the efficiency vs. bias current curve is effectively smeared out due to the oscillating bias current. Although the efficiency of the SNSPD without RF was 65%, the RF effectively reduces the peak efficiency to 48%, still significantly better than a PMT.

The motional heating rate of the ion is also affected by the presence of the SNSPD. When in trap zone B away from the SNSPD, the heating rate was 63 quanta/s at a frequency of 2 MHz. In zone D directly over the SNSPD, the heating rate was 113 quanta/s at a frequency of 5.3 MHz. It is unclear whether this increase in motional heating is due to noise on the SNSPD bias line, to material properties of the SNSPD or SiO_2 underneath it, or to some other mechanism. Nevertheless, these rates are still very comparable to the best results reported in cryogenic ion traps.

The high efficiency of the SNSPD combined with the low dark count rates allow an improvement in both readout speed and fidelity. An average readout fidelity of 0.9991 with a mean readout duration of 46 μs was demonstrated. Further details regarding state preparation and readout can be found in [111]. These results provide a path for scalable qubit readout in ion traps which could be used for quantum computing, quantum network nodes, or multi-ion optical clocks.

C. Waveguide Integration

Within the last decade there has been significant progress in scaling down of benchtop nonlinear setups into photonic integrated circuits. Chip-scale generation, manipulation and detection of quantum light has evolved from few-component photonic circuits to arrays of heralded single-photon sources and reconfigurable devices for multidimensional entanglement [112]. One key component is the waveguide-integrated single-photon detector.

In addition to avoiding losses from coupling off chip, these evanescently-coupled photon detectors offer a number of benefits compared to normal-incidence devices, including efficient detection over a wide range of wavelengths [113], arbitrary placement of a detector within a planar circuit, and allow in principle fast feedforward operations, if all detection, decision, and photon routing is performed on chip. In addition, the undetected signal is transmitted forward in the waveguide, meaning that a detector of low efficiency η is equivalent to a beam splitter-detector system with a splitting ratio of $(1-\eta)/\eta$ with an ideal detector of 100% efficiency on the η-coupling arm. This capability is of great significance to quantum optics applications involving heralding or photon subtraction as well as metrology applications [56].

One of the applications of waveguide-integrated SNSPDs at NIST has been development of advanced computing platforms such as neuromorphic computing, with hardware that mimics

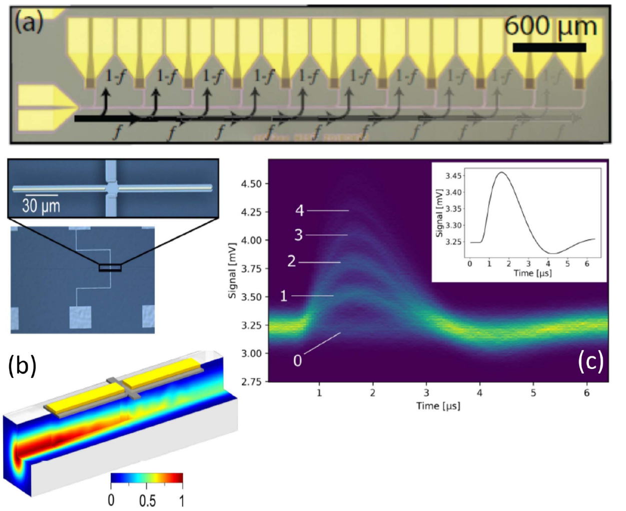

Fig. 12. (a) Optical microscope image of the HiDRA, designed to split off a fraction of the light to each of the 11 SNSPD detectors. Reproduced from [114]. (b) TES detector with extended absorbers utilizes a gold spine to increase thermal conduction and allow absorbed energy (from photons) to be detected by the TES (square device, center). Simulated mode profile as light propagating in the waveguide is absorbed by the TES detector due to evanescent coupling. Reproduced from [116]. (c) Measured photon traces with a TES evanescently coupled to lithium niobate waveguide showing different peak heights corresponding to different photon numbers per pulse. The inset shows the average TES response. Reproduced from [117].

the architecture of the brain. The platform includes waveguide integrated semiconductor light emitters coupled through reconfigurable nanophotonic waveguides and micro-ring filter banks to integrated detectors [114], [115].

To demonstrate the scalability of LEDs (Light-Emitting Diode) and SNSPDs, a device with a SiN waveguide integrated W-center LED in Si coupled to eleven WSi SNSPDs was demonstrated. An optical microscope image of such a device is shown in Fig. 12(a). This device consists of an LED (on the left) that couples into a waveguide with a series of power taps. At each tap, a fraction, f, of the light is directed to subsequent detectors, while $1 - f$ of the light goes to the nanowire detector at that port and so the n^{th} detector will receive $(1 - f)f^{n-1}$ of the light, assuming consistent power taps and detectors. This high-dynamic-range detector array (HiDRA) is useful for characterizing the operation of the LED over a broad range of current injection level.

By multiplexing or arraying SNSPDs on waveguides, it has been shown that quasi-photon-number resolving capabilities can be achieved in integrated photonic devices [118]. An alternative is to use a TES detector. High-efficiency photon-number resolving detectors that are waveguide-integrated, have been realized by adding absorption fins to W TES detectors on top of silica waveguides, as shown in Fig. 12(b). The absorption fins provide increased absorption area for the evanescently coupled light. The fins consist of patterned W film for light absorption and Au pads on top that provide increased thermal conduction of heat in the center active TES area. By multiplexing three TES detectors in series and using an on-chip terminal reflection grating, a detection efficiency of 88% $\pm$ 3% at 1550 nm wavelength was obtained [116].

Recently, proof-of-principle compatibility of evanescently coupled detectors with in-diffused lithium niobate waveguide platform has been demonstrated. Both integration of TES [117] detectors with photon number resolution up to six photons, (see Fig. 12(c)), and SNSPD [119] detectors with saturated quantum efficiency have been demonstrated.

D. Mid-Infrared Single-Photon Detection

The mid-infrared spectrum is relatively unfamiliar to most of the quantum optics community. Most experiments are performed in the telecommunications bands where the infrastructure is already well established. However, recently there has been interest in SNSPDs for their sensitivity at wavelengths beyond 1.55 μm, namely the 2–20 μm range, for applications which require sensitivity at the single-photon level.

One potential application of SNSPDs in this wavelength range is exoplanet spectroscopy. When a planet passes between its parent star and an observing telescope, part of the starlight passes through the planet's atmosphere. Spectroscopy of this light gives information about the content of the atmosphere, namely the concentrations of water (6.3 μm), methane (3.3 and 7.7 μm), ozone (9.6 μm), carbon monoxide (4.8 μm), carbon dioxide (4.3 μm and 15 μm), and nitrous oxide (4.5, 7.8, and 8.6 μm), which could be indicative of the presence of biological life. However, due to the extraordinarily small amount of starlight that passes through the atmosphere of the planet and eventually reaches the telescope, there are stringent requirements placed on the detectors used in this application in terms of both stability and noise. Stability is crucial because the spectrum must be integrated over several transits of the planet, with each transit typically lasting several hours or longer. Stability refers to stability of the detector gain, which for SNSPDs is flat as a function of bias current in the plateau region of the efficiency curve. Noise is also a critical factor, due to the weak spectral absorption features which must be resolved. With intrinsic dark count rates below 10^{-5} cps [105]. Furthermore, since the electrical pulse is effectively a digital signal, there is zero associated readout noise. This is in contrast to other mid-infrared detector technologies such as blocked impurity band (BIB) detectors and mercury cadmium telluride (MCT) detectors. Although both of those technologies are available in large-format arrays and operate at higher temperatures than SNSPDs, they have significantly higher dark count rates and non-zero readout noise.

To date, saturation of the internal detection efficiency has been demonstrated up to a wavelength of 10 μm [120]. SNSPDs optimized for the mid-infrared are fabricated differently than near-IR SNSPDs. In order to obtain saturation of the internal detection efficiency, the size of the hotspot created by the absorption of a photon must be comparable to the width of the nanowire. Thus, there are two potential paths to improving sensitivity-reducing the geometric cross section of the nanowire (making it thinner or narrower), or changing the properties of the material itself to obtain a larger hotspot for a given geometric cross section. Of these two approaches, the latter is preferable since yield is adversely affected as the width of the nanowire is reduced.

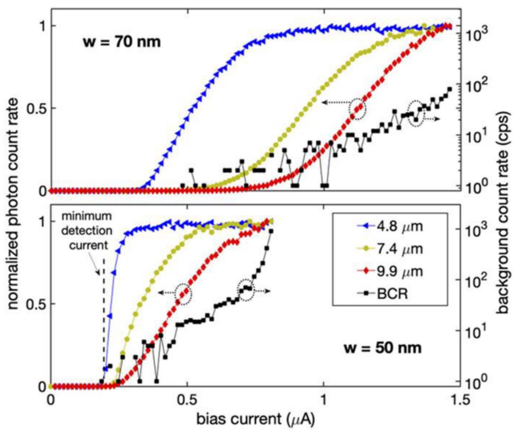

Fig. 13. Normalized photon count rate vs bias current curves for SNSPDs fabricated from a WSi film with a silicon content of 48% $\pm$ 10%. Two different nanowire widths (50 and 70 nm) are presented, and measurements were obtained at three wavelengths (4.8, 7.4, and 9.9 μm) at an operating temperature of 0.85 K. Black squares correspond to the measurement of the background count rates.

In theory, we expected a film with a higher resistivity to have a larger hotspot because the energy of the photon is divided amongst fewer electrons. Thus the average temperature of each electron should be higher for a given amount of energy deposited by the photon. This approach allows us to use wires that are wider than 50 nm, which enhances their overall yield.

An amorphous WSi film with higher resistivity can be obtained simply by increasing the silicon content of the film. The increased silicon content also lowers the film's critical temperature and critical current, requiring operation at lower bias currents and temperatures than traditional near-IR SNSPDs. Fig. 13 shows count rate vs. bias current curves for detectors fabricated from a high Si-content film with a silicon composition of 48% $\pm$ 10% at several different wavelengths. Typical silicon composition for near-IR SNSPDs is 20–25%. Two different nanowire widths are also shown, 50 nm and 70 nm. The photon count rate vs. bias current curves demonstrate saturated internal efficiency even at a wavelength of 9.9 μm. Note that the switching current is nearly an order of magnitude smaller than typical near-IR SNSPDs. This necessitates the use of cryogenic amplifiers for the SNSPD readout. Further reduction of the superconducting transition temperature and operating temperature, and increase of the silicon content, could potentially result in saturated efficiency up to a wavelength of 20 μm.

Another potential application of mid-infrared SNSPDs is quantum and free space optical communications. The mid-wave infrared (3–5 μm) has superior transmission through the atmosphere compared to visible, near infrared, short-wave infrared and long-wave infrared, and would suffer less from attenuation due to fog and atmospheric turbulence [121]. Mid-infrared SNSPDs could also potentially be useful in remote sensing applications in which blackbody radiation alone is used for navigation of a vehicle, eliminating the need for active illumination of a target or scene.

E. Quantum Metrology

One application of photon-number resolving TES detectors is enabling generation of entangled quantum states with multiple photons in high-dimensional spaces for exploring quantum phenomena in mesoscopic regime. The technique relies on the use of conditional measurements to engineer the excitation mode of the field through the simultaneous subtraction of photons from two-mode squeezed vacuum states. In [122], the generated states are composed of two multiphoton wave packets (up to ten photons) which are highly correlated and exhibit nearly Poissonian statistics. This achievement constitutes an important step towards the development of entangled laser-like beams.

Using pulsed measurements in the wavelength range of QD-based photon sources (653–932 nm), it was shown that TES detectors can discriminate photon number states up to 25 photons [123]. This opens up new possibilities for the analysis and exploration of solid-state-based quantum light sources for applications in quantum information, quantum-enhanced sensing and quantum metrology.

Another recent application of the PNR capability is investigation of photon number statistics of bimodal lasers using two TES detectors and their joint Photon Number Distribution. Using this technique, hopping between emission dynamics that are either associated with Poissonian or with thermal-like statistics was revealed [124].

F. Quantum Computing With Continuous Variables

Photons are the information carriers in the photonic quantum computing platforms. In the case of discrete-variable qubit-based implementations using single-photon states, the information can be encoded for example, in the photon polarization state [125]. However, many quantum variables, such as position, momentum, or the quadrature amplitudes of electromagnetic fields, are continuous, leading to the concept of continuous variables (CV). The amount of information carried in each CV can be much larger than that in a qubit [126].

For continuous-variable (CV) quantum information processing [126], [127], it is essential to generate CV entanglement which can be efficiently produced using squeezed light (in which the squeezing of a quadrature's quantum fluctuations is due to a nonlinear optical interaction [128] and linear optics. In general, squeezing refers to the reduction of quantum fluctuations in one observable below the standard quantum limit (the minimal noise level of the vacuum state) at the expense of an increased uncertainty of the conjugate variable.

Recently, quantum computational advantage (performing sampling tasks that are intractable for classical computers) with photons has been demonstrated by Gaussian Boson Sampling, where 100 single-photon detectors based on SNSPDs were used [129]. Boson Sampling is a mathematical proof that a many-photon state, when acted on by a large linear optical circuit will give rise to a probability distribution that cannot be efficiently sampled by a classical algorithm. For example, simulating the following quantum experiment: input n bosons in different modes of an m-mode ($m > n$) linear interferometer and sample events from the output distribution in the photon number basis at the interferometer's output modes [130]. Using single-photon detectors with no PNR capability, one can perform only approximate calculations. Replacing the single-photon detectors with PNR detectors would essentially advance such

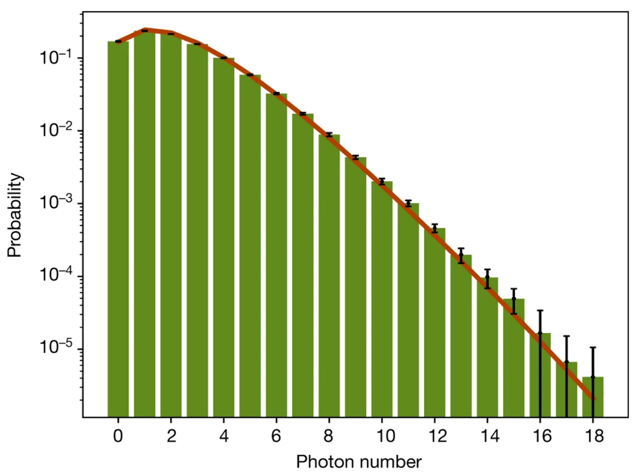

Fig. 14. Total photon-number distribution. All squeezers are turned on and the interferometer is set to identity. Estimates of the probabilities obtained from experimental samples are shown as bars. The theoretical prediction appears as a continuous line. Error bars denote one standard deviation taken over 12 runs of 10^5 samples. Reproduced from [48].

research. As a result, one of the key components for a photonic fault-tolerant universal quantum computer is a PNR detector that could be easily incorporated into real experimental systems [40], [127].

Recently [48], many-photon quantum circuit operations have been demonstrated using an integrated nanophotonics chip that generates strongly squeezed vacuum states on-chip coupled to a fully general programmable four-mode interferometer and uses TES based PNR readout on all outputs. Detection of multi-photon events with photon numbers and rates exceeding any previous programmable quantum optical demonstration was made possible by strong squeezing and high sampling rates. An example of the photon number states detected in the experiment is illustrated in Fig. 14, which shows the probability distribution for the total number of photons measured. In the implementation, the device is configured according to three different interferometers randomly selected from the Haar measure, generating 1.2×10^6 samples for each. The TES devices used in this experiment have larger than 95% quantum efficiency at 1550 nm wavelength. Up to 7 maximum number of photons were detected by TES devices with high photon-number resolving capability, such that photon number overlap probabilities of less than 10^{-3} were routinely measured.

In addition to demonstrating the non-classicality of the device output, the platform was used to carry out proof-of-principle demonstrations of three quantum algorithms: Gaussian boson sampling, molecular vibronic spectra and graph similarity. The demonstrations validated the platform as a viable path to scaling photonic technologies for multi-photon quantum information processing.

G. Nuclear-Decay Calorimetry

SNSPDs are sensitive to highly-localized energy implantation resulting in a cascading dissociation of electron-electron Cooper pairs within the superconducting film. This can occur from diverse types of processes not limited to photon absorption [105]. For example, SNSPDs can detect kinetic bombardment by massive particles such as atoms or ions. Furthermore, once such particles are embedded into or on the nanowire, the devices can sense subsequent decay of the particles to less-energetic internal states. These properties are proving useful in bounding the energy measurement of a Thorium-229 isomeric nuclear transition.

Atomic nuclei have internal excited states much like the bound electrons in an atom do. Thorium-229 (^{229}Th) is a relatively stable isotope of Thorium that is known to have a nuclear excited state that is optically accessible from the ground state [131]. The energy of this transition has been theoretically estimated by various groups to be between 7.6–7.8 $\pm$ 0.5 eV [132], [133], which corresponds to UV photon energies in the 150–170 nm wavelength range. More recent experimental efforts have narrowed the range to within 149–153 nm [134], [135]. There is consensus that the linewidth of the transition is 10–100 μHz, implying a Q-factor of 10^{19}. This isomer, when embedded in a crystal lattice at sufficient densities, could enable the creation of a "nuclear clock" that would be stable to better than 3 ns in a year [136]. The exact transition energy remains to be constrained in a range narrow enough for direct optical probing with a UV-comb laser to become viable.

A bulk source of Uranium-233 (^{233}U) is known to emit high-energy $^{229}\mathrm{Th}^{3+}$ ions in its radioactive α-decay. Some proportion of these ions (about 2%) are statistically expected to be in the first nuclear-excited state. In ions, the excited state can last for about $\sim$60 seconds. When the ^{229}Th atoms are neutralized via embedding into a bulk solid, the lifetime of the first nuclear excited state decreases to $<$10 μs. A stream of such ions have been filtered from the ^{223}U decay products in a mass spectrometer [137], and the lifetime of the excited state in ^{229}Th atoms neutralized on a multichannel plate (MCP) was found to be (7 $\pm$ 1) μs [138]. This was measured by analyzing time-correlated events that match spatial coordinates transverse to the beam. The MCP however, could not resolve the energy of the transition with significant precision.

SNSPDs have been shown to be able to spatially resolve the hotspot-creation location when integrated with a grounding plane and readout differentially using impedance-matched tapers [101], [139]. This method has been used in the time-of-flight multiplexing scheme for array readouts. In addition, the device-sensitivity-versus-current-bias curve for any given device is dependent on the energy deposited in the hotspot creation event, allowing SNSPDs to function as spectrometers [140]. These two abilities are being put to use in a new class of SNSPD-based microstrip imagers in order to probe the energy of the ^{229}Th nuclear transition. Such imagers have already shown an excess over background in spatio-temporally correlated decay events in the LMU Munich-based mass-spectrometer setup [137], and are being directly exposed to ^{233}U decay products in a collaborative effort with Hudson group at UCLA [141]–[143]. Similar efforts are ongoing at NIST [144].

IV. Conclusion

In this paper, we have presented a review of the key performance metrics for single-photon detectors for quantum information processing, as well as some recent advances in achieving them in superconducting photon-detection technologies. We have made a case for TESs and SNSPDs showing superior performance characteristics, justifying their wide adoption in quantum applications. A few cutting-edge research experiments have been presented.

Recent applications in quantum computing have pushed the requirements for even faster optical TES detectors while maintaining photon-number resolution. In addition to detector readout improvements and device thermal engineering that have speedup TES recovery time, fabrication improvements such as membrane release and fundamental detector design changes including material changes, may be required in the near future. Also, for quantum information as well as quantum microscopy a larger number of detectors will be required, hence optical TES array development. Readout development based on previous multiplexing approach for TES arrays using microwave superconducting quantum interference devices (SQUIDs), as well as novel integrated frequency-domain multiplexed readout will have the extra challenge to maintaining high system-detection efficiency and speed achieved for single pixel optical TESs.

With SNSPDs, the use of double-ended readout and impedance matching tapers has allowed large-area, high efficiency single-pixels to be realized without a degradation in jitter, which was previously impossible. However, a tradeoff still exists between detector size (and thus efficiency) and maximum count rate. Recent advances in the deposition of materials with fast electrothermal time constants such as NbN and NbTiN are helping to improve maximum count rates even for relatively large area detectors. Active reset circuits are currently being developed at NIST to improve maximum count rates even for large area detectors fabricated using amorphous superconductors which have slow electrothermal time constants. These circuits actively turn off the bias current to the detector as soon as the nucleation of the hotspot is detected by the circuit, allowing significantly faster reset times and a reduction in Joule heating. The development of ultra-low-noise amplifiers for readout of mid-infrared-sensitive SNSPDs is also of great interest, which could also be used to reducing the component of jitter associated with amplifier noise. Finally, larger array sizes continue to be demonstrated thanks to the development of new readout schemes and improved fabrication techniques. This is an exciting development that will likely have important future applications in fields such as astronomy, particularly in the UV and mid-infrared.

References

[1] D. V. Morozov, A. Casaburi, and R. H. Hadfield, "Superconducting photon detectors," *Contemporary Phys.*, vol. 62, no. 2, pp. 69–91, 2021.

[2] M. Tinkham, *Introduction to Superconductivity*, 2nd ed., New York, NY, USA: McGraw-Hill, 1995.

[3] J. Bardeen, L. N. Cooper, and J. R. Schrieffer, "Theory of superconductivity," *Phys. Rev.*, vol. 108, no. 5, pp. 1175–1204, 1957.

[4] B. Cabrera, R. M. Clarke, P. Colling, A. J. Miller, S. Nam, and R. W. Romani, "Detection of single infrared, optical, and ultraviolet photons using superconducting transition edge sensors," *Appl. Phys. Lett.*, vol. 73, no. 6, pp. 735–737, 1998.

[5] G. N. Gol'tsman et al., "Picosecond superconducting single-photon optical detector," *Appl. Phys. Lett.*, vol. 79, no. 6, pp. 705–707, 2001.

[6] A. Peacock et al., "Single optical photon detection with a superconducting tunnel junction," *Nature*, vol. 381, pp. 135–137, 1996.

[7] K. K. Likharev, "Superconducting weak links," *Rev. Mod. Phys.*, vol. 51, pp. 101–159, 1979.

[8] D. D. E. Martin and P. Verhoeve, "Superconducting tunnel junctions," *ISSI Sci. Rep. Ser.*, vol. 9, pp. 441–457, 2010.

[9] D. D. E. Martin, P. Verhoeve, T. Oosterbroek, R. Hijmering, A. Peacock, and R. Schulz, "Accurate time-resolved optical photospectroscopy with superconducting tunnel junction arrays," *Proc. SPIE*, vol. 6269, 2006, Art. no. 62690O.

[10] E. D. Walsh et al., "Josephson junction infrared single-photon detector," *Science*, vol. 372, pp. 409–412, 2021.

[11] B. A. Mazin et al., "Archons: A highly multiplexed superconducting optical to near-IR camera," *Proc. SPIE*, vol. 7735, 2000, Art. no. 773518.

[12] P. Szypryt et al., "Large-format platinum silicide microwave kinetic inductance detectors for optical to near-IR astronomy," *Opt. Exp.*, vol. 25, pp. 25894–25909, 2017.

[13] W. Guo et al., "Counting near infrared photons with microwave kinetic inductance detectors," *Appl. Phys. Lett.*, vol. 110, 2017, Art. no. 212601.

[14] N. Zobrist et al., "Design and performance of hafnium optical and near-IR kinetic inductance detectors," *Appl. Phys. Lett.*, vol. 115, 2019, Art. no. 213503.

[15] K. D. Irwin and G. C. Hilton, "Transition-edge sensors," in *Cryogenic Particle Detection*. Berlin/Heidelberg, Germany: Springer, 2005, pp. 63–150.

[16] J. N. Ullom and D. A. Bennett, "Review of superconducting transition-edge sensors for X-ray and gamma-ray spectroscopy," *Supercond. Sci. Technol.*, vol. 28, 2005, Art. no. 084003.

[17] R. C. Jaklevic, J. Lambe, A. H. Silver, and J. E. Mercereau, "Quantum interference effects in Josephson tunneling," *Phys. Rev. Lett.*, vol. 12, pp. 159–160, 1964.

[18] K. D. Irwin, "An application of electrothermal feedback for high resolution cryogenic particle detection," *Appl. Phys. Lett.*, vol. 66, pp. 1998–2000, 1995.

[19] A. E. Lita, A. J. Miller, and S. W. Nam, "Counting near-infrared single-photons with 95% efficiency," *Opt. Exp.*, vol. 16, pp. 3032–3040, 2008.

[20] M. Audley et al., "SCUBA-2: A large-format TES array for submillimetre astronomy," *Nucl. Instrum. Methods Phys. Res. Sect. A: Accelerators, Spectrometers, Detectors Assoc. Equip.*, vol. 520, pp. 479–482, 2004.

[21] R. den Hartog et al., "Low-noise readout of TES detectors with baseband feedback frequency domain multiplexing," *J. Low Temp. Phys.*, vol. 167, pp. 652–657, 2012.

[22] J. J. Renema et al., "Experimental test of theories of the detection mechanism in a nanowire superconducting single photon detector," *Phys. Rev. Lett.*, vol. 112, 2014, Art. no. 117604.

[23] A. Engel, J. Lonsky, X. Zhang, and A. Schilling, "Detection mechanism in SNSPD: Numerical results of a conceptually simple, yet powerful detection model," *IEEE Trans. Appl. Supercond.*, vol. 25, no. 5, Jun. 2015, Art. no. 2200407.

[24] P. C. Humphreys et al., "Tomography of photon-number resolving continuous-output detectors," *New J. Phys.*, vol. 17, 2015, Art. no. 103044.

[25] W. Zhang et al., "A 16-pixel interleaved superconducting nanowire single-photon detector array with a maximum count rate exceeding 1.5 GHz," *IEEE Trans. Appl. Supercond.*, vol. 29, no. 5, Aug. 2019, Art. no. 2200204.

[26] B. Korzh et al., "Demonstration of sub-3 ps temporal resolution with a superconducting nanowire single-photon detector," *Nature Photon.*, vol. 14, pp. 250–255, 2020.

[27] A. J. Miller, A. E. Lita, B. Calkins, I. Vayshenker, S. M. Gruber, and S. W. Nam, "Compact cryogenic self-aligning fiber-to-detector coupling with losses below one percent," *Opt. Exp.*, vol. 19, pp. 9102–9110, 2011.

[28] E. A. Dauler et al., "Review of superconducting nanowire single-photon detector system design options and demonstrated performance," *Opt. Eng.*, vol. 53, 2014, Art no. 081907.

[29] H. Wang et al., "Multispectral superconducting nanowire single-photon detector based on thickness-modulated optical film stack," *IEEE Photon. J.*, vol. 14, no. 2, pp. 1–4, Apr. 2022.

[30] X. Hou et al., "Ultra-broadband microfiber-coupled superconducting single-photon detector," *Opt. Exp.*, vol. 27, pp. 25241–25250, 2019.

[31] D. Fukuda et al., "Titanium-based transition-edge photon number resolving detector with 98% detection efficiency with index-matched small-gap fiber coupling," *Opt. Exp.*, vol. 19, pp. 870–875, 2011.
[32] D. V. Reddy, R. R. Nerem, S. W. Nam, R. P. Mirin, and V. B. Verma, "Superconducting nanowire single-photon detectors with 98% system detection efficiency at 1550 nm," *Optica*, vol. 7, pp. 1649–1653, 2020.
[33] P. Hu et al., "Detecting single infrared photons toward optimal system detection efficiency," *Opt. Exp.*, vol. 28, pp. 36884–36891, 2020.
[34] J. Chang et al., "Detecting telecom single photons with $99.5^{+0.5}_{-2.07}\%$ system detection efficiency and high time resolution," *APL Photon.*, vol. 6, 2021, Art. no. 036114.
[35] B. A. Mazin et al., "ARCONS: A 2024 pixel optical through near-IR cryogenic imaging spectrophotometer," *Publ. Astronomical Soc. Pacific*, vol. 125, pp. 1348–1361, 2013.
[36] L. Lolli, E. Taralli, and M. Rajteri, "Ti/Au TES to discriminate single photons," *J. Low Temp. Phys.*, vol. 167, pp. 803–808, 2012.
[37] L. A. Morais et al., "Precisely determining photon-number in real-time," 2020, *arXiv:2012.10158*.
[38] D. Zhu et al., "Resolving photon numbers using a superconducting nanowire with impedance-matching taper," *Nano Lett.*, vol. 20, pp. 3858–3863, 2020.
[39] L. Stasi, G. Gras, R. Berrazouane, and F. Bussieres, "High-efficiency and fast photon-number-resolving SNSPD,"in *Proc. Quantum Inf. Meas. VI*, 2021, Paper M2B.5.
[40] M. Endo et al., "Quantum detector tomography of a superconducting nanostrip photon-number-resolving detector," *Opt. Exp.*, vol. 29, pp. 11728–11738, 2021.
[41] R. Kobayashi, K. Hattori, S. Inoue, and D. Fukuda, "Development of a fast response titanium–gold bilayer optical TES with an optical fiber self-alignment structure," *IEEE Trans. Appl. Supercond.*, vol. 29, no. 5, pp. 1–5, Aug. 2019.
[42] M. Tarkhov et al., "Ultrafast reset time of superconducting single photon detectors," *Appl. Phys. Lett.*, vol. 92, 2008, Art. no. 241112.
[43] D. Fukuda et al., "Titanium TES based photon number resolving detectors with 1 mhz counting rate and 65% quantum efficiency," *Proc. SPIE*, vol. 7236, 2009, Art. no. 72360C.
[44] A. Lamas-Linares et al., "Nanosecond-scale timing jitter for single photon detection in transition edge sensors," *Appl. Phys. Lett.*, vol. 102, 2013, Art. no. 231117.
[45] J. Dreyling-Eschweiler, N. Bastidon, B. Döbrich, D. Horns, F. Januschek, and A. Lindner, "Characterization, 1064 nm photon signals and background events of a tungsten TES detector for the ALPS experiment," *J. Modern Opt.*, vol. 62, pp. 1132–1140, 2015.
[46] H. Shibata, K. Fukao, N. Kirigane, S. Karimoto, and H. Yamamoto, "SNSPD with ultimate low system dark count rate using various cold filters," *IEEE Trans. Appl. Supercond.*, vol. 27, no. 4, pp. 1–4, Jun. 2017.
[47] E. E. Wollman et al., "UV superconducting nanowire single-photon detectors with high efficiency, low noise, and 4 K operating temperature," *Opt. Exp.*, vol. 25, pp. 26792–26801, 2017.
[48] J. M. Arrazola et al., "Quantum circuits with many photons on a programmable nanophotonic chip," *Nature*, vol. 591, pp. 54–60, 2021.
[49] R. W. Romani, A. J. Miller, B. Cabrera, S. W. Nam, and J. M. Martinis, "Phase-resolved crab studies with a cryogenic transition-edge sensor spectrophotometer," *Astrophys. J.*, vol. 563, pp. 221–228, 2001.
[50] E. E. Wollman et al., "Kilopixel array of superconducting nanowire single-photon detectors," *Opt. Exp.*, vol. 27, pp. 35279–35289, 2019.
[51] B. Calkins, A. E. Lita, A. E. Fox, and S. Woo Nam, "Faster recovery time of a hot-electron transition-edge sensor by use of normal metal heat-sinks," *Appl. Phys. Lett.*, vol. 99, 2011, Art. no. 241114.
[52] T. Yamashita, K. Waki, S. Miki, R. A. Kirkwood, R. H. Hadfield, and H. Terai, "Superconducting nanowire single-photon detectors with non-periodic dielectric multilayers," *Sci. Rep.*, vol. 6, pp. 1–7, 2016.
[53] M. Perrenoud et al., "Operation of parallel SNSPDs at high detection rates," *Supercond. Sci. Technol.*, vol. 34, 2021, Art. no. 024002.
[54] H. Shibata, T. Honjo, and K. Shimizu, "Quantum key distribution over a 72 dB channel loss using ultralow dark count superconducting single-photon detectors," *Opt. Lett.*, vol. 39, pp. 5078–5081, 2014.
[55] D. Rosenberg et al., "Near-unity absorption of near-infrared light in tungsten films," *Nucl. Instrum. Methods Phys. Res. A*, vol. 520, pp. 537–540, 2004.
[56] T. Gerrits, A. E. Lita, B. Calkins, and S.-W. Nam, "Superconducting transition edge sensors for quantum optics," in *Superconducting Devices in Quantum Optics*, R. H. Hadfield and G. Johansson, Eds., Cham, Switzerland: Springer, ch. 2, 2016.
[57] D. Fukuda et al., "Titanium superconducting photon-number-resolving detector," *IEEE Trans. Appl. Supercond.*, vol. 21, no. 3, pp. 241–245, Jun. 2011.
[58] G. Fujii, D. Fukuda, T. Numata, A. Yoshizawa, H. Tsuchida, and S. Inoue, "Thin gold covered titanium transition edge sensor for optical measurement," *J. Low Temp. Phys.*, vol. 167, pp. 1573–7357, 2012.
[59] A. E. Lita, B. Calkins, L. A. Pellochoud, A. J. Miller, and S.-W. Nam, "High-efficiency photon-number-resolving detectors based on hafnium transition-edge sensors," in *Proc. AIP Conf.*, 2009, vol. 1185, pp. 351–354.
[60] A. Lita et al., "Tuning of tungsten thin film superconducting transition temperature for fabrication of photon number resolving detectors," *IEEE Trans. Appl. Supercond.*, vol. 15, no. 2, pp. 3528–3531, Jun. 2005.
[61] D. V. Reddy, N. Otrooshi, S. W. Nam, R. P. Mirin, and V. B. Verma, "Broadband polarization insensitivity and high detection efficiency in high-fill-factor superconducting microwire single-photon detectors," *APL Photon.*, vol. 7, 2022, Art. no. 0 51302.
[62] V. B. Verma, F. Marsili, S. Harrington, A. E. Lita, R. P. Mirin, and S. W. Nam, "A three-dimensional, polarization-insensitive superconducting nanowire avalanche photodetector," *Appl. Phys. Lett.*, vol. 101, 2012, Art. no. 251114.
[63] R. Baghdadi et al., "Enhancing the performance of superconducting nanowire-based detectors with high-filling factor by using variable thickness," *Supercond. Sci. Technol.*, vol. 34, 2021, Art. no. 035010.
[64] J.-M. Xiong et al., "Reducing current crowding in meander superconducting strip single-photon detectors by thickening bends," *Supercond. Sci. Technol.*, vol. 35, no. 5, 2022, Art. no. 055015.
[65] M. Jönsson et al., "Current crowding in nanoscale superconductors within the Ginzburg–Landau model," *Phys. Rev. Appl.*, vol. 17, 2022, Art. no. 064046.
[66] L. K. Shalm et al., "Strong loophole-free test of local realism," *Phys. Rev. Lett.*, vol. 115, 2015, Art. no. 250402.
[67] F. Ghafari et al., "Dimensional quantum memory advantage in the simulation of stochastic processes," *Phys. Rev. X*, vol. 9, 2019, Art. no. 041013.
[68] L. K. Shalm et al., "Device-independent randomness expansion with entangled photons," *Nature Phys.*, vol. 17, pp. 452–456, 2021.
[69] K. Wei, W. Zhang, Y.-L. Tang, L. You, and F. Xu, "Implementation security of quantum key distribution due to polarization-dependent efficiency mismatch," *Phys. Rev. A*, vol. 100, 2019, Art. no. 022325.
[70] D. V. Reddy, R. R. Nerem, A. E. Lita, S. W. Nam, R. P. Mirin, and V. B. Verma, "Exceeding 95% system efficiency within the telecom C-band in superconducting nanowire single photon detectors," in *Proc. Conf. Lasers Electro-Opt.*, 2019, pp. 1–2.
[71] Y. Meng et al., "Fractal superconducting nanowires detect infrared single photons with 84% system detection efficiency, 1.02 polarization sensitivity, and 20.8 ps timing resolution," *ACS Photon.*, vol. 5, pp. 1547–1553, 2022.
[72] G.-Z. Xu et al., "Superconducting microstrip single-photon detector with system detection efficiency over 90% at 1550 nm,"*Photon. Res.*, vol. 9, pp. 958–957, 2021.
[73] Y. P. Korneeva et al., "Different single-photon response of wide and narrow superconducting Mo $_x$ Si_{1-x} strips," *Phys. Rev. Appl.*, vol. 13, 2020, Art. no. 024011.
[74] J. Chiles et al., "Superconducting microwire detectors based on WSi with single-photon sensitivity in the near-infrared," *Appl. Phys. Lett.*, vol. 116, 2020, Art. no. 242602.
[75] D. Vodolazov, N. Manova, Y. Korneeva, and A. Korneev, "Timing jitter in NbN superconducting microstrip single-photon detector," *Phys. Rev. Appl.*, vol. 14, 2020, Art. no. 044041.
[76] I. Charaev, Y. Morimoto, A. Dane, A. Agarwal, M. Colangelo, and K. K. Berggren, "Large-area microwire MoSi single-photon detectors at 1550 nm wavelength," *Appl. Phys. Lett.*, vol. 116, 2020, Art. no. 242603.
[77] A. E. Lita, V. B. Verma, J. Chiles, R. P. Mirin, and S. W. Nam, "Mo $_x$ Si_{1-x}: A versatile material for nanowire to microwire single-photon detectors from UV to near IR," *Supercond. Sci. Technol.*, vol. 34, 2021, Art. no. 054001.
[78] S. Steinhauer, S. Gyger, and V. Zwiller, "Progress on large-scale superconducting nanowire single-photon detectors," *Appl. Phys. Lett.*, vol. 118, 2021, Art. no. 100501.
[79] L. You, "Superconducting nanowire single-photon detectors for quantum information," *Nanophotonics*, vol. 9, pp. 2673–2692, 2020.
[80] N. Calandri, Q.-Y. Zhao, D. Zhu, A. Dane, and K. K. Berggren, "Superconducting nanowire detector jitter limited by detector geometry," *Appl. Phys. Lett.*, vol. 109, 2016, Art. no. 152601.

[81] A. G. Kozorezov et al., "Fano fluctuations in superconducting-nanowire single-photon detectors," *Phys. Rev. B*, vol. 96, 2017, Art. no. 054507.
[82] J. J. Renema et al., "Position-dependent local detection efficiency in a nanowire superconducting single-photon detector," *Nano Lett.*, vol. 15, pp. 4541–4545, 2015.
[83] D. Y. Vodolazov, "Minimal timing jitter in superconducting nanowire single-photon detectors," *Phys. Rev. Appl.*, vol. 11, 2019, Art. no. 014016.2019, Art. no. 014016.
[84] Y. Cheng, C. Gu, and X. Hu, "Inhomogeneity-induced timing jitter of superconducting nanowire single-photon detectors," *Appl. Phys. Lett.*, vol. 111, 2017, Art. no. 062604.
[85] H. Wu, C. Gu, Y. Cheng, and X. Hu, "Vortex-crossing-induced timing jitter of superconducting nanowire single-photon detectors," *Appl. Phys. Lett.*, vol. 111, 2017, Art. no. 062603.
[86] M. Sidorova et al., "Physical mechanisms of timing jitter in photon detection by current-carrying superconducting nanowires," *Phys. Rev. B*, vol. 96, 2017, Art. no. 184504.
[87] J. Allmaras, A. Kozorezov, B. Korzh, K. Berggren, and M. Shaw, "Intrinsic timing jitter and latency in superconducting nanowire single-photon detectors," *Phys. Rev. Appl.*, vol. 11, 2019, Art. no. 034062.
[88] A. D. Semenov, "Superconducting nanostrip single-photon detectors some fundamental aspects in detection mechanism, technology and performance," *Supercond. Sci. Technol.*, vol. 34, 2021, Art. no. 054002.
[89] B. Cabrera, "Introduction to tes physics," *J. Low Temp. Phys.*, vol. 151, pp. 82–93, 2008.
[90] P. Ravindran, R. Cheng, H. Tang, and J. C. Bardin, "Active quenching of superconducting nanowire single photon detectors," *Opt. Exp.*, vol. 28, pp. 4099–4114, 2020.
[91] A. J. Kerman, J. K. W. Yang, R. J. Molnar, E. A. Dauler, and K. K. Berggren, "Electrothermal feedback in superconducting nanowire single-photon detectors," *Phys. Rev. B*, vol. 79, 2009, Art. no. 100509.
[92] A. J. Kerman, D. Rosenberg, R. J. Molnar, and E. A. Dauler, "Readout of superconducting nanowire single-photon detectors at high count rates," *J. Appl. Phys.*, vol. 113, 2013, Art. no. 144511.
[93] D. Rosenberg, A. J. Kerman, R. J. Molnar, and E. A. Dauler, "High-speed and high-efficiency superconducting nanowire single photon detector array," *Opt. Exp.*, vol. 21, pp. 1440–1447, 2013.
[94] D. Rosenberg, A. E. Lita, A. J. Miller, and S. W. Nam, "Noise-free high-efficiency photon-number-resolving detectors," *Phys. Rev. A*, vol. 71, 2005, Art. no. 061803.
[95] D. Fixsen, S. Moseley, B. Cabrera, and E. Figueroa-Feliciano, "Pulse estimation in nonlinear detectors with nonstationary noise," *Nucl. Instrum. Methods. Phys. Res. A*, vol. 520, pp. 555–558, 2004.
[96] Z. H. Levine et al., "Algorithm for finding clusters with a known distribution and its application to photon-number resolution using a superconducting transition-edge sensor," *J. Opt. Soc. Amer. B*, vol. 29, pp. 2066–2073, 2012.
[97] D. J. Fixsen, S. H. Moseley, T. Gerrits, A. E. Lita, and S. W. Nam, "Optimal energy measurement in nonlinear systems: An application of differential geometry," *J. Low Temp. Phys.*, vol. 176, pp. 16–26, 2014.
[98] T. Gerrits et al., "Extending single-photon optimized superconducting transition edge sensors beyond the single-photon counting regime," *Opt. Exp.*, vol. 20, pp. 23798–23810, 2012.
[99] C. Cahall et al., "Multi-photon detection using a conventional superconducting nanowire single-photon detector," *Optica*, vol. 4, pp. 1534–1535, 2017.
[100] S. Sempere-Llagostera, G. S. Thekkadath, R. B. Patel, W. S. Kolthammer, and I. A. Walmsley, "Reducing $g^{(2)}(0)$ of a parametric down-conversion source via photon-number resolution with superconducting nanowire detectors," *Opt. Exp.*, vol. 30, pp. 3138–3147, 2022.
[101] M. Colangelo et al., "Impedance-matched differential superconducting nanowire detectors," 2021, *arXiv:2108.07962*.
[102] W. L. Stutzman and G. Thiele, "Wire antennas," in *Antenna Theory and Design*. Hoboken, NJ, USA: Wiley, 2012, pp. 177.
[103] E. A. Dauler et al., "Photon-number-resolution with sub-30-ps timing using multi-element superconducting nanowire single photon detectors," *J. Modern Opt.*, vol. 56, pp. 364–373, 2009.
[104] R. Cheng, Y. Zhou, S. Wang, M. Shen, T. Taher, and H. X. Tang, "Unveiling photon statistics with a 100-pixel photon-number-resolving detector," 2022, *arXiv:2206.13753*.
[105] J. Chiles et al., "New constraints on dark photon dark matter with superconducting nanowire detectors in an optical haloscope," *Phys. Rev. Lett.*, vol. 128, 2022, Art. no. 231802.
[106] J. P. Allmaras et al., "Demonstration of a thermally coupled row-column snspd imaging array," *Nano Lett.*, vol. 20, pp. 2163–2168, 2020.
[107] A. N. McCaughan et al., "The thermally-coupled imager: A scalable readout architecture for superconducting nanowire single photon detectors," 2021, *arXiv:2112.04705*.
[108] S. Doerner et al., "Frequency-multiplexed bias and readout of a 16-pixel superconducting nanowire single-photon detector array," *Appl. Phys. Lett.*, vol. 111, 2017, Art. no. 032603.
[109] S. Miyajima, M. Yabuno, S. Miki, T. Yamashita, and H. Terai, "High-time-resolved 64-channel single-flux quantum-based address encoder integrated with a multi-pixel superconducting nanowire single-photon detector," *Opt. Exp.*, vol. 26, pp. 29045–29054, 2018.
[110] T. Konno, S. Takasu, K. Hattori, and D. Fukuda, "Development of an optical transition-edge sensor array," *J. Low Temp. Phys.*, vol. 199, pp. 27–33, 2020.
[111] S. L. Todaro et al., "State readout of a trapped ion qubit using a trap-integrated superconducting photon detector," *Phys. Rev. Lett.*, vol. 126, 2021, Art. no. 010501.
[112] G. Moody, L. Chang, T. J. Steiner, and J. E. Bowers, "Chip-scale nonlinear photonics for quantum light generation," *AVS Quantum Sci.*, vol. 2, 2020, Art. no. 041702.
[113] M. A. Wolff et al., "Broadband waveguide-integrated superconducting single-photon detectors with high system detection efficiency," *Appl. Phys. Lett.*, vol. 118, 2021, Art. no. 154004.
[114] S. Buckley et al., "All-silicon light-emitting diodes waveguide-integrated with superconducting single-photon detectors," *Appl. Phys. Lett.*, vol. 111, 2017, Art. no. 141101.
[115] J. M. Shainline et al., "Room-temperature-deposited dielectrics and superconductors for integrated photonics," *Opt. Exp.*, vol. 25, pp. 10322–10334, 2017.
[116] B. Calkins et al., "High quantum-efficiency photon-number-resolving detector for photonic on-chip information processing," *Opt. Exp.*, vol. 21, pp. 22657–22670, 2013.
[117] J. P. Höpker et al., "Integrated transition edge sensors on titanium in-diffused lithium niobate waveguides," *APL Photon.*, vol. 4, 2019, Art. no. 056103.
[118] D. Sahin et al., "Waveguide photon-number-resolving detectors for quantum photonic integrated circuits," *Appl. Phys. Lett.*, vol. 103, 2013, Art. no. 111116.
[119] J. P. Höker et al., "Integrated superconducting detectors on titanium in-diffused lithium niobate waveguides," *Conf. Lasers Electro-Opt.*, 2020, *Paper FF3D.6*.
[120] V. B. Verma et al., "Single-photon detection in the mid-infrared up to 10 μm wavelength using tungsten silicide superconducting nanowire detectors," *APL Photon.*, vol. 6, 2021, Art. no. 056101.
[121] L. Flannigan, L. Yoell, and C. Q. Xu, "Mid-wave and long-wave infrared transmitters and detectors for optical satellite communications–a review," *J. Opt.*, vol. 24, 2022, Art. no. 043002.
[122] O. S. Magaña-Loaiza et al., "Multiphoton quantum-state engineering using conditional measurements," *npj Quantum Inf.*, vol. 52019.
[123] M. Schmidt et al., "Photon-number-resolving transition-edge sensors for the metrology of quantum light sources," *J. Low Temp. Phys.*, vol. 193, pp. 1243–1250, 2018.
[124] M. Schmidt et al., "Bimodal behavior of microlasers investigated with a two-channel photon-number-resolving transition-edge sensor system," *Phys. Rev. Res.*, vol. 3, 2021, Art. no. 013263.
[125] J. Carolan et al., "Universal linear optics," *Science*, vol. 349, pp. 711–716, 2015.
[126] S. Lloyd and S. L. Braunstein, "Quantum computation over continuous variables," *Phys. Rev. Lett.*, vol. 82, pp. 1784–1787, 1999.
[127] S. Takeda and A. Furusawa, "Toward large-scale fault-tolerant universal photonic quantum computing," *APL Photon.*, vol. 4, 2019, Art. no. 060902.
[128] D. F. Walls and G. J. Milburn, *Quantum Optics*. Berlin/Heidelberg, Germany: Springer2008.
[129] H.-S. Zhong et al., "Quantum computational advantage using photons," *Science*, vol. 370, pp. 1460–1463, 2020.
[130] S. Aaronson and A. Arkhipov, "The computational complexity of linear optics," in *Proc. 43rd Annu. ACM Symp. Theory Comput.*, 2011, pp. 333–342.
[131] L. A. Kroger and C. W. Reich, "Features of the low-energy level scheme of ^{229}Th as observed in the α-decay of ^{233}U," *Nucl. Phys. A*, vol. 259, pp. 29–60, 1976.

[132] B. R. Beck et al., "Energy splitting of the ground-state doublet in the nucleus ^{229}Th," *Phys. Rev. Lett.*, vol. 98, 2007, Art. no. 142501.

[133] E. V. Tkalya, C. Schneider, J. Jeet, and E. R. Hudson, "Radiative lifetime and energy of the low-energy isomeric level in ^{229}Th," *Phys. Rev. C*, vol. 92, 2015, Art. no. 054324.

[134] B. Seiferle et al., "Energy of the ^{229}Th nuclear clock transition," *Nature*, vol. 573, pp. 243–246, 2019.

[135] T. Sikorsky et al., "Measurement of the ^{229}Th isomer energy with a magnetic microcalorimeter," *Phys. Rev. Lett.*, vol. 125, 2020, Art. no. 142503.

[136] W. G. Rellergert, D. DeMille, R. R. Greco, M. P. Hehlen, J. R. Torgerson, and E. R. Hudson, "Constraining the evolution of the fundamental constants with a solid-state optical frequency reference based on the ^{229}Th nucleus," *Phys. Rev. Lett.*, vol. 104, 2010, Art. no. 200802.

[137] L. von der Wense et al., "Direct detection of the ^{229}Th nuclear clock transition," *Nature*, vol. 533, pp. 47–51, 2016.

[138] B. Seiferle, L. von der Wense, and P. G. Thirolf, "Lifetime measurement of the ^{229}Th nuclear isomer," *Phys. Rev. Lett.*, vol. 118, 2017, Art. no. 042501.

[139] Q.-Y. Zhao et al., "Single-photon imager based on a superconducting nanowire delay line," *Nature Photon.*, vol. 11, pp. 247–251, 2017.

[140] L. Kong et al., "Single-detector spectrometer using a superconducting nanowire," *Nano Lett.*, vol. 21, pp. 9625–9632, 2021.

[141] E. Hudson, "Quantum science seminar #48 - eric hudson," 2021. [Online]. Available: https://www.youtube.com/watch?v=Ez0470tcw6s

[142] R. Elwell et al., "Superconducting nanowire spectroscopy of the ^{229}Th isomer," in *Proc. 53rd Annu. Meeting APS Division At., Mol. Opt. Phy.*, 2022, vol. 67, no. 7.

[143] R. Elwell et al., "Search efforts for the ^{229}Th isomeric transition," in *Proc. APS Division At., Mol. Opt. Phy. Meeting Abstr.*, 2022.

[144] S. Patra, B. Seiferle, D. V. Reddy, S. W. Nam, D. Leibrandt, and G. O'Neil, "Towards an improved measurement of the 8 eV Thorium-229 nuclear isomer transition energy using a superconducting detector," in *Proc. 53rd Annu. Meeting APS Division At., Mol. Opt. Phy.*, 2022, vol. 67, no. 7.